JGR Oceans

RESEARCH ARTICLE
10.1029/2023JC020401

Special Collection:
Physical processes, sediment transport and morphodynamics of estuaries and coastal seas

Localized Tidal Energy Extraction in Puget Sound Can Adjust Estuary Reflection and Friction, Modifying Barotropic Tides System-Wide

Preston Spicer[1], Parker MacCready[2], and Zhaoqing Yang[1,3]

[1]Coastal Sciences Division, Pacific Northwest National Laboratory, Seattle, WA, USA, [2]School of Oceanography, University of Washington, Seattle, WA, USA, [3]Department of Civil and Environmental Engineering, University of Washington, Seattle, WA, USA

Key Points:

- A large, hypothetical tidal stream turbine farm is simulated to investigate the impact of tidal energy extraction on Salish Sea tides
- Tidal energy fluxes are calculated throughout the system and decomposed into incident and reflected components
- The turbine farm adds frictional dissipation, which modifies how the M_2 and K_1 tides reflect and propagate in slightly different ways

Correspondence to:
Z. Yang,
Zhaoqing.Yang@pnnl.gov

Citation:
Spicer, P., MacCready, P., & Yang, Z. (2024). Localized tidal energy extraction in Puget Sound can adjust estuary reflection and friction, modifying barotropic tides system-wide. *Journal of Geophysical Research: Oceans*, *129*, e2023JC020401. https://doi.org/10.1029/2023JC020401

Received 29 AUG 2023
Accepted 19 APR 2024

Author Contributions:
Conceptualization: Preston Spicer, Parker MacCready, Zhaoqing Yang
Data curation: Preston Spicer
Formal analysis: Preston Spicer
Funding acquisition: Zhaoqing Yang
Investigation: Preston Spicer
Methodology: Preston Spicer, Parker MacCready, Zhaoqing Yang
Project administration: Zhaoqing Yang
Resources: Parker MacCready, Zhaoqing Yang
Software: Zhaoqing Yang
Supervision: Parker MacCready, Zhaoqing Yang

Abstract Harvesting energy via tidal stream turbines is being increasingly considered as a renewable energy resource in estuaries with strong tidal currents. It remains unclear how localized energy extraction changes basic tidal physics throughout real systems. Here, we analyze the influence of an extensive synthetic tidal turbine array on barotropic tides in the Salish Sea, a complex, tidally energetic estuary, using a realistic numerical model. Tidal energy fluxes are calculated at 15 sections throughout the system and decomposed into incident and reflected components, as well as by frequency. Results show the dominant semidiurnal constituent, M_2, controls the total tidal energy flux everywhere. When turbines are placed in Tacoma Narrows, the M_2 energy flux is enhanced at sections seaward of the array in Puget Sound and reduced landward. The principal diurnal constituent, K_1, contributes little to the total energy flux, but behaves similarly. Changes to each constituent are primarily attributed to turbine enhanced frictional dissipation which reduces the estuary's natural resonant period (~10 hr) amplification. Being close to the semidiurnal frequencies, the resonance adjustment reduces M_2 tidal reflection seaward of the turbines and free surface amplitude (particularly landward of the turbines) thereby increasing (decreasing) tidal energy fluxes at seaward (landward) locations. K_1 is further from the natural frequency and insensitive to resonance changes. We hypothesize K_1 is directly sensitive to increased frictional dissipation which acts to reduce reflection and tidal amplitude, regardless of the estuary natural frequency. Spatial variability in dynamics is discussed, as well as potential environmental implications.

Plain Language Summary Energy can be extracted from strong tidal currents present in many coastal estuaries via tidal stream turbines. We still lack a thorough understanding of how tidal turbine farms can modify tides and currents throughout the estuarine system they are installed in. Here, we use a computer model of the Salish Sea in the Pacific Northwest to simulate a large, synthetic tidal turbine farm in Tacoma Narrows to investigate impacts on tides elsewhere: from the Straits of Juan de Fuca and Georgia to South Puget Sound. We find that the tide occurring twice daily (M_2) is more energetic than the once daily (K_1) tide throughout the Salish Sea and so the M_2 is more important to the transfer of tidal energy through the estuary (tidal energy flux). Adding turbines modifies both tides by adding friction to the system. Both tides are reflected less throughout the estuary, and the M_2 tidal range is generally reduced. The turbines increase tidal energy fluxes at some locations and decrease it elsewhere. The findings of this hypothetical study highlight a sensitivity of Salish Sea tides to large scale energy extraction.

1. Introduction

Barotropic tides are a universal feature of many of the world's estuaries and coastal seas. Astronomical tidal cycles force predictable changes to sea surface elevations which can pulse huge volumes of water into and out of coastal embayments over semidiurnal (~12 hr) and diurnal (~24 hr) periods, with the strength of each tide modulated over even longer timescales (e.g., Doodson, 1921; Foreman & Henry, 1989; Godin, 1986). As such, a myriad of processes, both physical and biogeochemical, at numerous timescales are dictated or modified by tidal forcing. Time varying currents change in magnitude and direction depending on tidal phase and create turbulence through interactions with the rough sea bottom, channel sidewalls, or internal velocity shear (e.g., Geyer & Smith, 1987; Sleath, 1987). Bottom generated turbulence mixes the water column and suspend sediments, thereby adding turbidity to coastal waters, while currents transport and deposit the suspended or bedload sediments elsewhere (e.g., Allen et al., 1980; Burchard et al., 2018; Dyer, 1995). In the presence of horizontal and vertical salinity gradients induced by river inflow, tides contribute to even more complex dynamics, and act to help stratify or mix

Validation: Preston Spicer, Parker MacCready, Zhaoqing Yang
Visualization: Preston Spicer
Writing – original draft: Preston Spicer
Writing – review & editing: Preston Spicer, Parker MacCready, Zhaoqing Yang

the water column depending on tidal phase, and support the subtidal estuarine circulation, the process of drawing salty water into estuaries at depth to replace the export of fresher, mixed waters at the surface (Geyer & MacCready, 2014). Tidal interaction with stratification can also initiate the development of internal waves, which act to transfer momentum and mix buoyancy in the water column (e.g., Woodson, 2018). These processes, amongst others, play crucial roles in governing estuarine health, productivity, and morphology, and warrant continued research on barotropic tides in coastal systems.

In this paper, we investigate tidal dynamics within the Salish Sea: a large, complex system which comprises some of the inland coastal waters of Washington and British Columbia: namely, the Straits of Juan de Fuca and Georgia, as well as Puget Sound and its sub-basins (see Figure 1 for place names). Geographically, the Salish Sea can be considered a network of deep, fjord-like straits and basins, but unlike systems of similar geometry, behaves much like an estuary due to exceptional tidal and river forcing which contribute to locally vigorous mixing and a strong estuarine circulation (e.g., Bretschneider et al., 1985; MacCready et al., 2021; Sutherland et al., 2011; Thomson et al., 2007). Tidal forcing is as complex as the geography: mixed semidiurnal and diurnal constituents vary locally in relative strength, basin geometry supports progressive tidal waves entering the system and standing waves in the inland basins, and current magnitudes can vary greatly from near zero in wide basins to upwards of 8 m/s in some narrow straits (Lavelle et al., 1988; Mofjeld & Larsen, 1984; Sutherland et al., 2007; Yang et al., 2021). Tides in the Salish Sea support a generally healthy estuarine environment, but concerns do exist in some sub-basins, such as Hood Canal, where tidal currents and mixing are weak, and hypoxic conditions have persisted or even worsened in past decades (Curl & Paulson, 1991; Newton et al., 1995; Paulson et al., 2006).

Locally significant tidal currents within the Salish Sea have drawn attention to the region as a potential site for tidal energy extraction. Specifically, the narrow channels around Johnstone Strait, the San Juan Islands, and Puget Sound feature the strongest currents, and sections such as Tacoma Narrows, which connects the Main Basin to South Sound, has an estimated annual mean kinetic energy flux exceeding 50 MW (Yang et al., 2021), of which some percentage could be extractable as tidal power. It has been well established that tidal energy extraction can modify tidal water levels and currents both local to turbine placement and throughout entire estuarine systems (e.g., Hasegawa et al., 2011; Sánchez et al., 2014; Spicer et al., 2023; Ward et al., 2012; Yang et al., 2013), yet few studies isolate the physical mechanisms which drive these turbine-induced changes to hydrodynamics within real systems. Although a significant effort has been put forth in characterizing the tidal energy resource within the Salish Sea (e.g., Defne et al., 2012; Haas et al., 2011; Kilcher et al., 2016; Polagye et al., 2009; Sutherland et al., 2007; Yang et al., 2021), there has been disproportionally little work analyzing how tidal turbine farms may modify the important tidal processes there. Noteworthy exceptions are the studies by Yang et al. (2014) and Wang and Yang (2017) who investigated the local hydrodynamic response of turbine farms in some sub-basins of Puget Sound. Polagye et al. (2009) also analyzed how energy extraction in Admiralty Inlet and Tacoma Narrows may affect barotropic tides, transport, and energy dissipation elsewhere using an idealized, 1D channel model. They found both the M_2 and K_1 tides to be adjusted in differing ways depending on location. Yet, we still lack a mechanistic understanding of why local tidal energy extraction may modify barotropic tides throughout the full, realistic Salish Sea system, as well as physical explanations for spatial variability. Given the importance of tides to broader physical and biogeochemical processes here, we aim to address this gap in the present study.

A useful tool for describing the barotropic tide at a given location is the tidal energy flux. Both the potential and kinetic energy of the tidal wave are included, providing a metric for the total energy associated with the tide, which then may be used to characterize tidal propagation as well as free surface and current amplitudes. We can isolate the contributions of individual tidal constituents to the net energy flux, and as we will show in this paper, further decompose the net flux into incident and reflected tidal wave components. As such, the tidal energy flux can be quite helpful in understanding the basic physical processes dictating tidal behavior. Former studies have calculated tidal energy fluxes in portions of the Salish Sea to investigate the barotropic tide (Foreman et al., 1995; Lavelle et al., 1988), but there still is considerable uncertainty in how incident and reflected waves contribute to total energy fluxes and dissipation throughout all the basins. Moreover, it remains to be seen how tidal energy extraction will modify incident and reflected wave dynamics (important in near resonant systems like the Salish Sea) and what this means for the composite tide.

The goal of this study is to provide an evaluation of how significant tidal energy extraction in a single, energetic region of the Salish Sea may modify barotropic tidal dynamics elsewhere in the system, as well as identify the physical mechanisms responsible for changes. A more intensive background on tides in the Salish Sea is given in

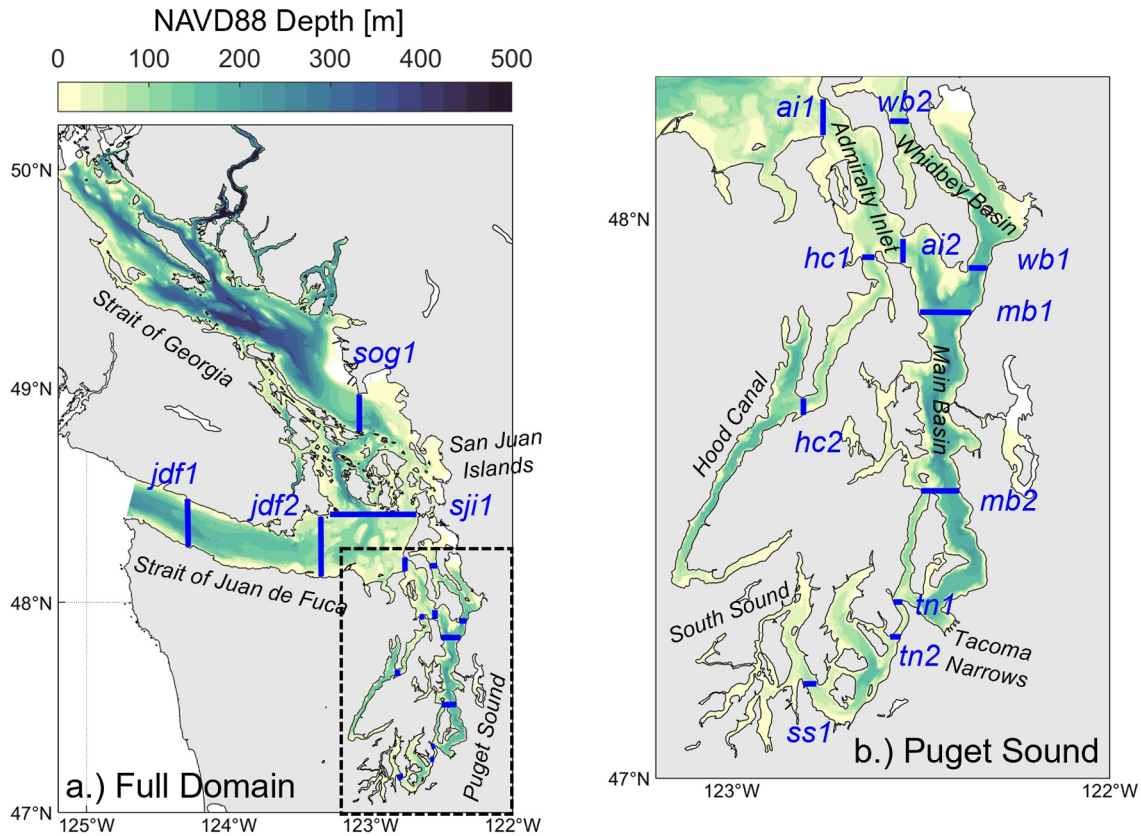

Figure 1. (a) Study area map showing the Salish Sea and basins. Depth is given as colored contours, with any region in white being outside the model domain. (b) Zoom-in on Puget Sound (dashed box in a). In both panels, sections used in the analysis are marked with blue lines and labeled. Basins and sub-basins are labeled in black.

Section 2. Since tidal turbines are yet to be deployed en masse in the Salish Sea, we utilize a realistic numerical model of the region and simulate a hypothetical turbine farm; the details of which are given in Section 3. In Section 4, we formulate the tidal energy flux and subsequent decomposition into incident and reflected components. Results comparing tidal energy fluxes in the system with and without tidal energy extraction are given in Section 5. We diagnose how the dominant diurnal and semidiurnal frequencies display different responses to turbines and discuss results in the context of estuary health in Section 6. Conclusions are presented last in Section 7.

2. Barotropic Tides in the Salish Sea

Friction and geometry are important, spatially varying controls on barotropic tidal dynamics in the Salish Sea. Depths are mainly quite deep (100s of meters) and basins are relatively wide, except for multiple connection points between sub-basins where sills (40–80 m deep) and reduced widths restrict flow considerably (Figure 1). It is at these locations, namely the San Juan Island channels, Admiralty Inlet, the entrance to Hood Canal, and Tacoma Narrows, where the most intense spatially varying change occurs in tides and currents (e.g., Ebbesmeyer & Barnes, 1980; Lavelle et al., 1988; Mofjeld & Larsen, 1984). The changes are created partly by frictional forces which are orders of magnitude larger at the constrictions than the deeper, wider basins they connect, enhanced from increased bottom drag but more so by form drag initiated by rapid changes in flow acceleration due to channel geometry and flow separation (e.g., Edwards et al., 2004; MacCready et al., 2003; McCabe et al., 2006). Friction leads to significant energy dissipation at the constrictions, while geometry often allows partial reflection of the tidal wave, leading to modulation of the barotropic tide which often manifests as an increase in phase lag over each constriction but enhanced tidal amplitudes (Lavelle et al., 1988). In the following paragraphs, we present a synopsis of the current understanding of barotropic tidal dynamics in the basins and narrow straits which comprise the Salish Sea, elaborating on the changes mentioned above.

Tides enter the Salish Sea through the Juan de Fuca and Johnstone straits, the latter being a relatively small channel connecting the northern end of the Strait of Georgia to the Pacific Ocean. Subtidal exchange flows and tidal energy fluxes through Johnstone Strait are small relative to Juan de Fuca (exchange flow = 1/6 the magnitude (MacCready et al., 2021; Thompson, 1981) and energy fluxes = ¼ the magnitude (Sutherland et al., 2007)), and as such, the mouth of Juan de Fuca is considered the effective entryway for tidal forcing. A mixed-semidiurnal tide enters Juan de Fuca from the Pacific (form factor, $K = \frac{K_1+O_1}{M_2+S_2} < 1$) and is dominated by (in order of importance) the semidiurnal M_2 and diurnal K_1 constituents, with notable contributions from S_2, O_1, N_2, P_1, K_2, and Q_1 which behave dynamically similar to the M_2 (if semidiurnal) and K_1 (if diurnal) throughout. Broadly, both the M_2 and K_1 frequencies act as progressive waves in Juan de Fuca and characteristically transition to standing waves in the more reflective Strait of Georgia and Puget Sound where tidal phases are near constant. The largest phase differences occur through the San Juan Islands (~15 and ~30° for K_1 and M_2, respectively) and Admiralty Inlet (~10 and ~25°) with a smaller jump over Tacoma Narrows (~7 and ~10°). Minimum K_1 and M_2 amplitudes (~0.45 and ~0.4 m, respectively) occur at the western and eastern (near Victoria, B.C. where semidiurnal degenerate amphidromes exist) ends of Juan de Fuca, respectively, and amplify at constriction points in the San Juan Islands, Admiralty Inlet, and Tacoma Narrows, where partial reflection occurs, and at the northern end of the Strait of Georgia and South Sound, where more significant reflection occurs at the estuary limits. The M_2 amplifies the most in Puget Sound and is 2.2 times larger in South Sound than in Juan de Fuca, whereas the K_1 increases by a factor of 1.2. Conversely, in the Strait of Georgia, K_1 amplifies by a factor of 2 and the M_2 by 1.3 (Lavelle et al., 1988; Mofjeld & Larsen, 1984). The Juan de Fuca—Strait of Georgia system was found to behave nearest to a Helmholtz oscillator (although rectangular bay resonance theory was also tested) and has a resonant period between 17 (Helmholtz model) and 21 hr (rectangular), explaining the near constant phases landward of the San Juan Islands and large amplitudes of both the K_1 and M_2 tides there (Sutherland et al., 2005). Puget Sound, which comprises less than 10% of the Salish Sea volume, is thought to have a frequency response controlled by and similar to the much larger Juan de Fuca—Strait of Georgia system. Alternatively, the larger amplification of the M_2 tide in Puget Sound may suggest a lower resonant period closer to 12.42 hr, distinct from yet influenced by Juan de Fuca—Strait of Georgia which sets the incoming tidal condition to Puget Sound (e.g., Godin, 1993).

Tidal currents and transport in the Salish Sea are predominantly controlled by the M_2 frequency, with K_1 being roughly 40% smaller in magnitude (Lavelle et al., 1988). The strongest tidal currents (>3 m/s) occur in the Johnstone Strait, San Juan Islands, Admiralty Inlet, and Tacoma Narrows constrictions, as well as in South Sound (Foreman et al., 1995; Mofjeld & Larsen, 1984). Alternatively, weaker currents (<0.5 m/s) are forced in the wider Main Basin and Strait of Georgia, and nearly negligible tidal currents occur at the landward limits of Hood Canal and Whidbey Basin (LeBlond, 1983; Mofjeld & Larsen, 1984). K_1 currents and transport experience more frictional damping due to the dominating influence of M_2 currents on quadratic friction (Sutherland et al., 2005). This variable influence of friction likely causes the reduced K_1 transport and tidal prism in South Sound relative to that of M_2. In this paper, we show sensitivity to friction as an important control on how the K_1 tide behaves relative to M_2 when tidal turbines are modeled.

3. Tidal Model and Energy Extraction Setup

A tidal hydrodynamic model of the Salish Sea was previously developed to investigate tidal energy potential in the system (Yang et al., 2021) which we apply here to explore how tidal energy extraction may modify barotropic dynamics. The modeling framework used is the Finite-Volume Community Ocean Model (FVCOM) (Chen et al., 2003) which solves the 3-D Navier-Stokes equations of continuity and momentum. FVCOM is a general-purpose ocean model consisting of multiple sub-modules used to simulate numerous physical and biogeochemical processes in the coastal ocean and has been widely applied in modeling tidal energy extraction (e.g., Cowles et al., 2017; Li et al., 2017; Yang et al., 2013; Yang et al., 2014). FVCOM utilizes an unstructured grid modeling framework which is particularly useful for resolving complex estuary and coastline geometries.

The model grid resolution generally varies from ~500 m at the open boundaries to ~50 m in the narrow straits and channels of the San Juan Islands and Puget Sound, with some cells in the Strait of Georgia approaching 1,000 m. In Tacoma Narrows, where the hypothetical turbine array is ultimately placed, grid resolution is even finer at ~20 m. In total, there are approximately 843,000 nodes and 1,632,000 triangular elements. The model is forced with tides and river discharge for completeness, as river discharge can affect currents near river mouths, but over most of the domain tidal currents are not influenced in a meaningful way. Further, the baroclinic total exchange

flow through the system is largely driven by tidal pumping, not gravitational circulation induced by freshwater inflows (MacCready & Geyer, 2024), and so omission of river-induced stratification is likely not majorly consequential to modeled transport. In total, 19 major river discharges are included with daily flow rates acquired from the United States Geological Survey (USGS) and Environment Canada (for the Fraser River). The model open boundaries are located at the entrance of Juan de Fuca and the head of the Strait of Georgia, near Johnstone Strait (see Figure 1). As such, direct observations of tidal elevations measured at tide gauges in Neah Bay, Washington (Juan de Fuca entrance) and Campbell River, British Columbia (Johnstone Strait) were used to force tides in the model. All simulations were performed in 3D barotropic mode, allowing 3D flows to be simulated but omitting the influence of water density on currents and mixing, as barotropic dynamics are the focus of this work. Wind forcing was not included in these simulations to keep focus on the barotropic tide. Vertically, 10 uniform sigma layers were applied to resolve 3D flow structure. A Smagorinsky scheme was applied for horizontal mixing (Smagorinsky, 1963) and the Mellor-Yamada 2.5 turbulence closure scheme for vertical mixing of momentum (Mellor & Yamada, 1982). Bottom friction follows the quadratic law with the drag coefficient determined by the logarithmic bottom layer as a function of bottom roughness. A bottom roughness length of 0.001 m and friction coefficient of 0.0025 were applied throughout the model domain. A standard radiation boundary condition is applied at the open boundaries to allow river-added mass and volume to exit the domain (Chen et al., 2003). In this configuration, the Salish Sea tidal hydrodynamic model was validated extensively with currents at 132 moored Acoustic Doppler current profiler (ADCP) stations deployed by NOAA between 2015 and 2017, and water levels at 10 continuously operating NOAA and Department of Fisheries and Oceans Canada tide gauges. A more detailed description of model grid development, configuration, forcing, and validation can be found in Yang et al. (2021).

Modeling energy extraction via tidal turbines is a requirement of the current study. To achieve this, a current energy converter (CEC) module was implemented in FVCOM which applies the momentum sink approach in simulating the effect of turbines on flow (Rao et al., 2016; Yang et al., 2013). The method was used in an idealized estuary and validated with analytical solutions (Yang et al., 2013). The CEC module has proven useful in accurately simulating tidal energy extraction and physical-environmental impacts on the surrounding system (e.g., Haverson et al., 2018; O'Hara Murray & Gallego, 2017). In using the CEC module, the governing equations for Reynolds averaged turbulent flows are as follows (Yang et al., 2013):

$$\frac{\partial u}{\partial t}+u\frac{\partial u}{\partial x}+v\frac{\partial u}{\partial y}+w\frac{\partial u}{\partial z}-fv=-\frac{1}{\rho_0}\frac{\partial p}{\partial x}+\frac{\partial}{\partial z}\left(K_m\frac{\partial u}{\partial z}\right)+F_x-F_x^M \tag{1}$$

$$\frac{\partial v}{\partial t}+u\frac{\partial v}{\partial x}+v\frac{\partial v}{\partial y}+w\frac{\partial v}{\partial z}+fu=-\frac{1}{\rho_0}\frac{\partial p}{\partial y}+\frac{\partial}{\partial z}\left(K_m\frac{\partial v}{\partial z}\right)+F_y-F_y^M \tag{2}$$

where x, y, and z are the east, north, and vertical coordinates, respectively; u, v, and w are velocities corresponding to the x, y, and z directions; F_x and F_y are the horizontal momentum diffusivity terms in the x and y directions; K_m is the vertical eddy viscosity; ρ_0 is water density; p is pressure; and f is the Coriolis parameter. F_x^M and F_y^M are the additional momentum sink terms associated with energy extraction which are defined as:

$$\overrightarrow{F^M}=\frac{1}{2}\frac{C_eA_b}{V_c}\left|\vec{u}\right|\vec{u} \tag{3}$$

where V_c is the momentum control volume where the tidal turbine is located (volume of 3D grid cells turbine encompasses), C_e is the momentum extraction coefficient (and includes drag forces due to turbine poles, blades, foundation, and thrust force), A_b is the flow facing area swept by the turbine, and $\vec{u}$ is the velocity vector (u or v). In this work, C_e is directly prescribed as a constant 0.5 as we are not modeling any specific turbine design, but rather approximating the effect of generic turbines (e.g., Spicer et al., 2023; Yang et al., 2013). In iterative curve-fitting tests between modeled and observed turbine velocity profiles, Li et al. (2017) found C_e of 0.41 to match observations best, and so a similar value is used here. Further, De Dominicis et al. (2017) tested multiple C_e values on power extraction estimates and concluded that $C_e > 0.85$ is likely too liberal in energy extraction, and lesser values are most realistic.

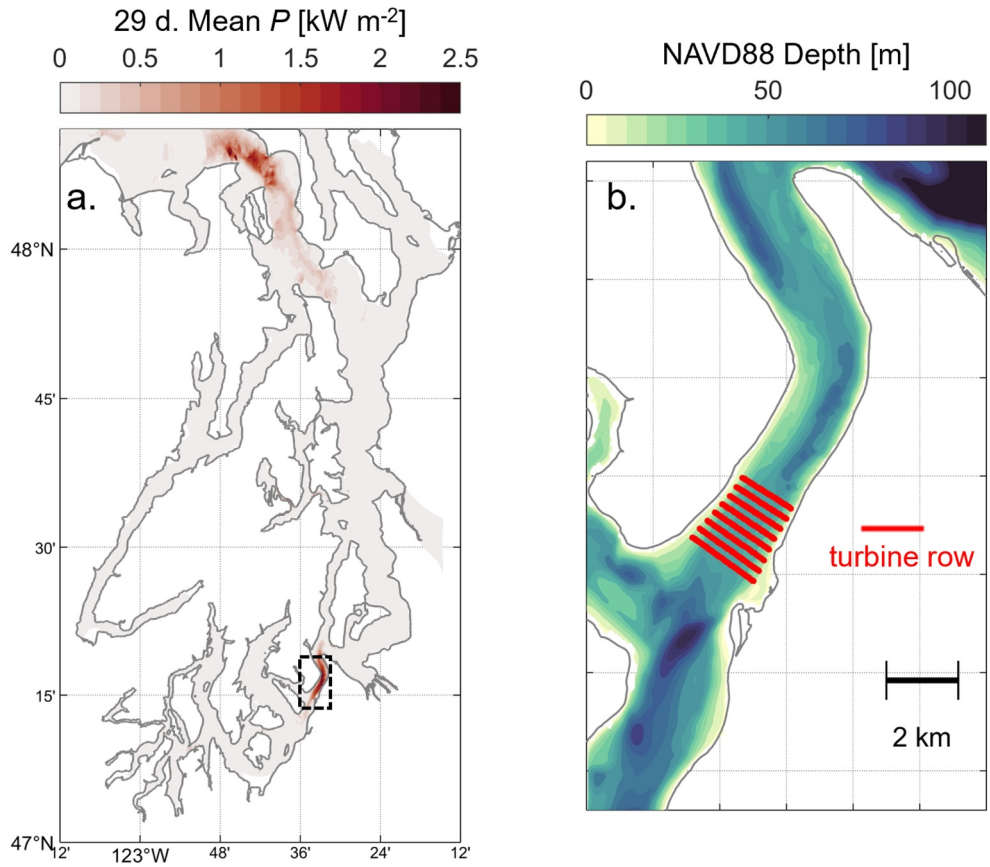

Figure 2. (a) Colored contour of 29-day mean power density in Puget Sound. (b) Zoom-in on Tacoma Narrows (dashed box in a) with colored contours of depth. The row locations of simulated tidal turbines are given are red lines.

A hypothetical tidal turbine array was simulated in Puget Sound using the CEC module, the location of which was determined by tidal power potential. Power potential was evaluated by calculating the power density, P (W m^{-2}), over the full domain:

$$P = 0.5\rho_0 V^3 \tag{4}$$

where V is the depth-averaged current speed. One 35-day simulation (06/01/2015 to 07/05/2015) of the validated Salish Sea model was run (to capture a full spring-neap cycle) with no turbines and Equation 4 was calculated at each grid cell at each time step then time averaged over the last 29 days (to omit model spin-up, see below). Figure 2a shows the 29-day mean power density over Puget Sound, where the largest magnitudes appeared. Significant tidal power density (~2 kW m^{-2}) was identified in Admiralty Inlet, with even larger magnitudes (~2.5 kW m^{-2}) in Tacoma Narrows (Figure 2a), two regions previously identified as potential tidal energy extraction points (Yang et al., 2014, 2021). We chose Tacoma Narrows as the best location to simulate a turbine array, as power densities are largest there while depths are consistently deep in the main channel (~50 m, Figure 2b) as to not disrupt shipping.

The simulated turbines were made 10 m in diameter with a center hub height 10 m from the seabed, a typical design employed in other recent energy extraction studies (Spicer et al., 2023; Yang et al., 2014). The modeled turbines were placed in rows bounded by the 20 m depth contour on either side, allowing a minimum 5 m clearance between turbine blades and surface, with considerably more clearance in the channel center where shipping traffic would be expected. Rows were spaced 10 rotor-diameters apart (200 m) to minimize downstream wake effects, while individual turbine lateral spacing was 2 rotor-diameters apart (20 m), similarly allowing lateral wake dissipation. Rows were placed in the lower reach of Tacoma Narrows where power densities are

largest, over a 1,400 m straight segment of the channel featuring nearly constant channel depths greater than 60 m, giving 7 rows and a total of 480 turbines (Figure 2b), a relatively dense turbine array.

A theoretical maximum annual-average power ($P_{\max}$) which may be extracted from Tacoma Narrows was derived following Garrett and Cummins (2005):

$$P_{\max} = \beta \rho_0 g a_0 Q_{\max} \left[1 + \frac{9}{16} \left(\sum_{i=1}^{M_t} \left(\frac{a_i}{a_0} \right)^2 \right) \right] \tag{5}$$

where g is gravitational acceleration, a_0 is the largest tidal constituent amplitude, and a_i ($i = 1, 2, \ldots, M_t$) are additional M_t tidal constituent amplitudes, $Q_{\max}$ is the maximum flow rate, and β is a time-dependence coefficient varying from 0.20 to 0.24 (which we took as 0.22). Taking all eight tidal constituent amplitudes and $Q_{\max}$ at the entrance of Tacoma Narrows (section *tn1*), $P_{\max}$ was estimated as 472 MW and the time mean (29 days) of extracted power from our array configuration is roughly 15% of that value at ~70 MW. Average extracted power values greater than 2% of $P_{\max}$ (9.4 MW in this case) classify the synthetic array as a large farm (IEC, 2015). Even so, thousands of turbines would be required to extract the total theoretical energy, beyond what is practical from regulatory and siting perspectives (Yang et al., 2013). Here, we simulate a large-scale turbine array to emphasize hydrodynamic impacts. Another 35-day simulation was run with this turbine configuration for the same period as the no turbine (base) case (06/01/2015 to 07/05/2015). For both the base and turbine cases output was created at 15 min intervals and results compared for the final 29 days, effectively providing a 6-day model ramp-up.

4. Tidal Energy Flux: Incident, Reflected, and Net

Tidal energy fluxes were calculated at 15 sections throughout the Salish Sea (labeled in Figure 1) for the net, incident, and reflected waves as well as for individual constituents. The 8 major semidiurnal and diurnal tidal frequencies which force the Salish Sea model were applied: M_2, S_2, N_2, K_2, K_1, O_1, P_1, and Q_1.

Our derivation and decomposition start with the linearized equations of momentum and mass, respectively, for cross sectionally averaged variables in a channel of uniform depth and width (channel dimensions discussed more, below):

$$\frac{\partial u_*}{\partial t} = -g \frac{\partial \eta_*}{\partial x} - \lambda u_* \tag{6}$$

$$\frac{\partial \eta_*}{\partial t} + H \frac{\partial u_*}{\partial x} = 0 \tag{7}$$

where u_* and η_* are the section-normal velocity and sea surface displacement, respectively, H is section depth, t is time, x is along-channel distance, and λ is the linear friction coefficient. Nonlinear terms are assumed to be small in the Salish Sea, as the relative magnitude of M_4 and M_6 overtide amplitudes to the M_2 (M_4/M_2 and M_6/M_2) are generally on the order of 0.01 and 0.001, respectively, supporting the linearized assumption.

In Equations 6 and 7, u_* and η_* may be decomposed as the net sum of the real parts of incident (+) and reflected (−) waves for each tidal constituent, j, over n total constituents, such that:

$$\eta_*(x,t) = \sum_{j=1}^{n} Re\left\{ A_+ e^{i(kx+\omega t)} + A_- e^{i(-kx+\omega t)} \right\}_j \tag{8}$$

$$u_*(x,t) = \sum_{j=1}^{n} Re\left\{ U_+ e^{i(kx+\omega t)} - U_- e^{i(-kx+\omega t)} \right\}_j \tag{9}$$

where ω is the angular frequency, A_+, A_-, U_+, and U_- are the incident and reflected complex free surface (A) and velocity (U) amplitudes, and k is the complex wavenumber, all of which vary for each constituent, j. k is derived from the equations of motion for channels of constant depth and width as:

$$k = \frac{\omega}{\sqrt{gH}}\sqrt{1 - i\frac{\lambda}{\omega}} \tag{10}$$

To determine A_+, A_-, U_+, and U_- for each constituent, we assume the total (incident plus reflected) complex amplitudes (A_o and U_o) are known at a given section, at which we set $x = 0$ for convenience, thereby quantifying the net wave as:

$$\eta_*(0,t) = \sum_{j=1}^{n} Re\{A_o e^{i\omega t}\}_j \tag{11}$$

$$u_*(0,t) = \sum_{j=1}^{n} Re\{U_o e^{i\omega t}\}_j \tag{12}$$

and then apply the relationships which relate Equations 8 and 9 to Equations 11 and 12:

$$A_+ + A_- = A_o \tag{13}$$

$$U_+ - U_- = U_o \tag{14}$$

$$\begin{cases} U_+ = \alpha A_+ \\ U_- = \alpha A_- \end{cases} \tag{15}$$

where the parameter α is:

$$\alpha = \frac{\sqrt{g/H}}{\sqrt{1 - i\frac{\lambda}{\omega}}} \tag{16}$$

We substitute each part of Equation 15 into Equation 14 which allows:

$$\alpha A_+ - \alpha A_- = U_o \tag{17}$$

thereby leading to the formulae for the complex amplitudes of incident and reflected waves in terms of the known amplitudes:

$$A_+ = \frac{A_o + (U_o/\alpha)}{2} \tag{18}$$

$$A_- = \frac{A_o - (U_o/\alpha)}{2} \tag{19}$$

with U_+ and U_- then being calculated using Equation 15.

Finally, corresponding tidal energy fluxes for the incident, reflected, and net waves (F_+, F_-, and F) of each constituent are expressed as:

$$F_+ = \frac{1}{2}\rho_0 g A_c [Re(A_+ U_+) + Im(A_+ U_+)] \tag{20}$$

$$F_- = -\frac{1}{2}\rho_0 g A_c [Re(A_- U_-) + Im(A_- U_-)] \tag{21}$$

$$F = \frac{1}{2}\rho_0 g A_c [Re(A_o U_o) + Im(A_o U_o)] \tag{22}$$

where A_c is the time-averaged area of a given section and Im denotes the imaginary part for the complex expression AU. We can quantify the energy fluxes for the composite tide by summing Equations 20–22 over all constituents. From here on, "composite" tide refers to the tidal wave reconstructed with all 8 major tidal constituents. Note: the composite tidal flux is not necessarily the "total" tidal flux, as the total would include nonlinear terms which are not included in a simple summation.

In this paper, harmonic analysis via UTide (Codiga, 2011) is performed on 29-day time series' of η_* and u_* at each section to determine A_o and U_o, respectively. Nodal tide corrections are applied, and phases are Greenwich-referenced. The P_1 and K_2 tidal harmonics are inferred from predetermined, observational relationships, as our short analysis period does not allow a completely accurate dissection of the P_1 from K_1 and K_2 from S_2 (see Foreman & Henry, 1989). We applied the following amplitude ratios: $A_{P1}/A_{K1} = 0.31$ and $A_{K2}/A_{S2} = 0.27$, and phase offsets: $\varphi_{K1} - \varphi_{P1} = 0.5°$ and $\varphi_{S2} - \varphi_{K2} = -0.6°$, for inference, which we calculated using amplitudes and phases provided by NOAA at eight tide gauges in the Salish Sea. We then averaged each ratio/offset over all eight stations to get one representative value. Applying inference reduced error in both amplitude and phase predictions for the P_1, K_1, K_2, and S_2 tides by up to 100% (not shown).

The linear friction coefficient, λ, is set to zero at each section as the real value is unknown and likely varies across the domain due to spatial variability in bottom drag, form drag, and currents. Only with zero friction is the sum of the incident and reflected fluxes ($F_+ + F_-$) equal to the original flux (described in next paragraph). Interestingly, this is not true of the sum of two waves traveling in the same direction, as is clear from consideration of a wave packet. Further, the approach taken in this paper assumes each section in Figure 1 represents the "mouth" of a different, uniform channel, defined by a set of complex sea surface and velocity amplitudes: A_o and U_o. As such, the influence of friction, as well as convergence/divergence from the inherently non-uniform regions between sections, is included in A_o and U_o, and therefore all tidal energy flux estimates. The complexity of topography in the Salish Sea warrants this general approach: both friction and convergence are highly variable throughout the system, and difficult to estimate with a direct application of theory (see Appendix A).

The original flux is calculated without harmonic decomposition as:

$$F_o = \overline{\rho_0 g A_c \eta_* u_*} \tag{23}$$

where the overbar denotes a temporal mean (29 days in this case, nearly an integer number of tidal cycles for all 8 forced constituents). This allows us to check the consistency of our incident-reflected decomposition. Here we find $F_+ + F_-$ is generally within ±10% of F_o. As Equation 23 is not reconstructed but rather uses raw model output, it includes more constituents (overtides and compound tides) than the 8 used in Equation 20 thru Equation 22 and typically slightly exceeds those estimates.

At all sections, positive u_* is taken as the up-estuary (landward) direction. As such, incident and net energy fluxes are landward directed (positive), while reflected are seaward (negative). Since FVCOM features an unstructured grid, currents and free surface elevations are interpolated onto section transect coordinates from adjacent nodes (free surface) and elements (currents) before section averaged to get η_* and u_*.

5. Results

5.1. Effects of Energy Extraction on Composite Tide

Incident, reflected, and net tidal energy fluxes at each section were checked and shown to agree favorably with former work (see Appendix B), validating our calculations and decomposition method. Next, we evaluated the difference in composite tidal energy fluxes for the base versus turbine cases to identify the influence of the turbines on tidal characteristics throughout the Salish Sea.

Results indicate tidal energy extraction in Tacoma Narrows has a minor influence on F in the straits of Juan de Fuca and Georgia (Figures 3a and d). The turbines have a more notable effect on dynamics within Puget Sound and its sub-basins. Along the main axis of Puget Sound from *ai1* to near the turbine array location (*tn2*), F magnitudes increase relative to the base case (Figure 3b). The enhancement in F increases gradually from *ai1* (+15 MW, or +5%) to a maximum at *tn1* (+52 MW, or +35%). Landward of the array in South Sound, F is decreased relative to the base case (−3 MW, or −7%) at *ss1* (Figures 3b and d). Smaller differences in F between

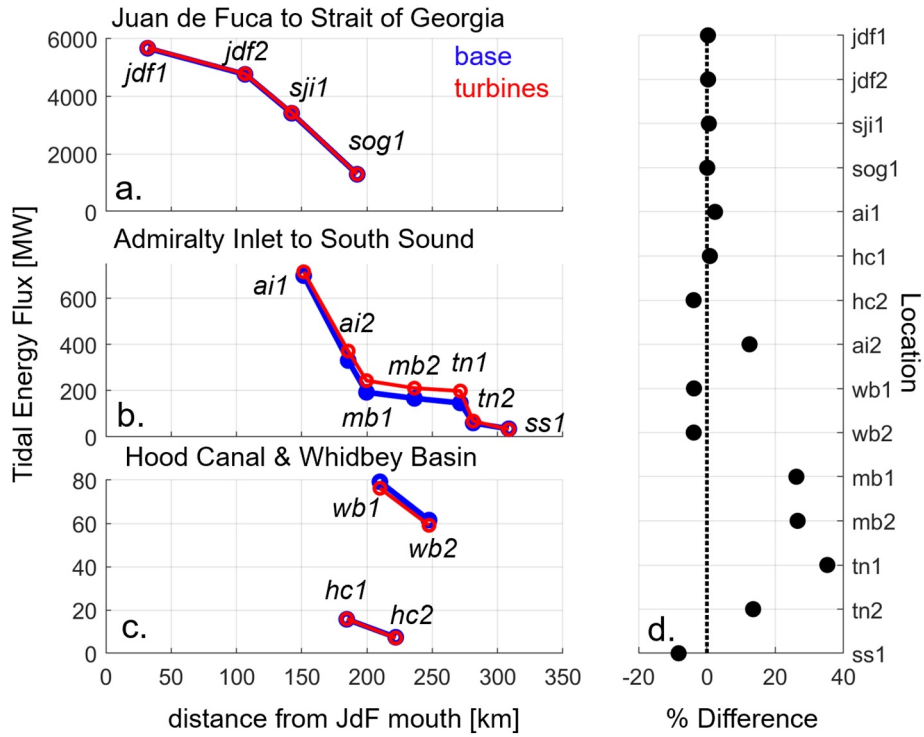

Figure 3. Comparison of net (left panels) tidal energy flux estimates for the base (blue) and turbines (red) simulations at sections in Juan de Fuca/Strait of Georgia (a), Admiralty Inlet to South Sound (b), and Hood Canal & Whidbey Basin (c). Distance from the mouth of Juan de Fuca is given on the *x*-axis and energy flux, in megawatts, on the *y*-axis. Section locations are labeled in each subplot. Percent difference (*x*-axis) of turbine case estimates relative to base are given at all locations (*y*-axis) on (d).

Admiralty Inlet and the entrance to Tacoma Narrows relative to the base case indicates less frictional dissipation occurs over the region, while the larger reduction in F between *tn1* and South Sound points to locally larger frictional dissipation in Tacoma Narrows, an expected result of the turbines which act as momentum sinks. Interestingly, F is also reduced in Hood Canal and Whidbey Basin (-10% at *hc1*, *wb1*, *wb2*) when tidal energy is extracted (Figures 3c and 3d), even though the basins they are attached to see increased F.

Decomposition of tidal energy fluxes into incident and reflected components provides more insight on variability in tidal modulation described above. Like net fluxes, most change occurs within Puget Sound relative to Juan de Fuca and the Strait of Georgia, where there is generally a less than 2% change in both F_+ and F_- (Figure 4d). At all sections along the main axis of Puget Sound seaward of the turbine array (*ai1* to *tn2*), turbines disproportionally decrease reflected energy fluxes over incident, which allows the increased net, landward fluxes described in Figure 3. The deviation between the relative differences in F_+ and F_- grows moving from *ai1* (reflected: -5%, incident: -3%) to a maximum at *tn1* (reflected: -13%, incident: $\sim 0\%$), aligning with patterns of gradually enhanced F approaching Tacoma Narrows (Figure 4d). Landward of the turbines (South Sound), as well as in Hood Canal and Whidbey Basin, incident and reflected fluxes are reduced nearly equally (generally -3% to -7%), supporting decreased F in those sub-basins (Figure 4d). These results suggest the presence of turbines in Tacoma Narrows can modify tides on both the landward and seaward sides of the array, with seaward dynamics mainly modified via reduced reflected energy.

5.2. Effects of Energy Extraction on M_2 and K_1 Tides

Increased dissipation of tidal energy initiated by the turbine farm clearly modifies tidal propagation by reducing reflection in most of Puget Sound and damping the tidal energy entering South Sound, Hood Canal, and Whidbey Basin. The numerous frequencies comprising the composite tide may behave differently to adjustments in both friction and reflection. Evaluating the contributions of the major semidiurnal (M_2) and diurnal (K_1) constituents to F is therefore necessary to identify the importance of each to the composite tidal energy flux and identify the role

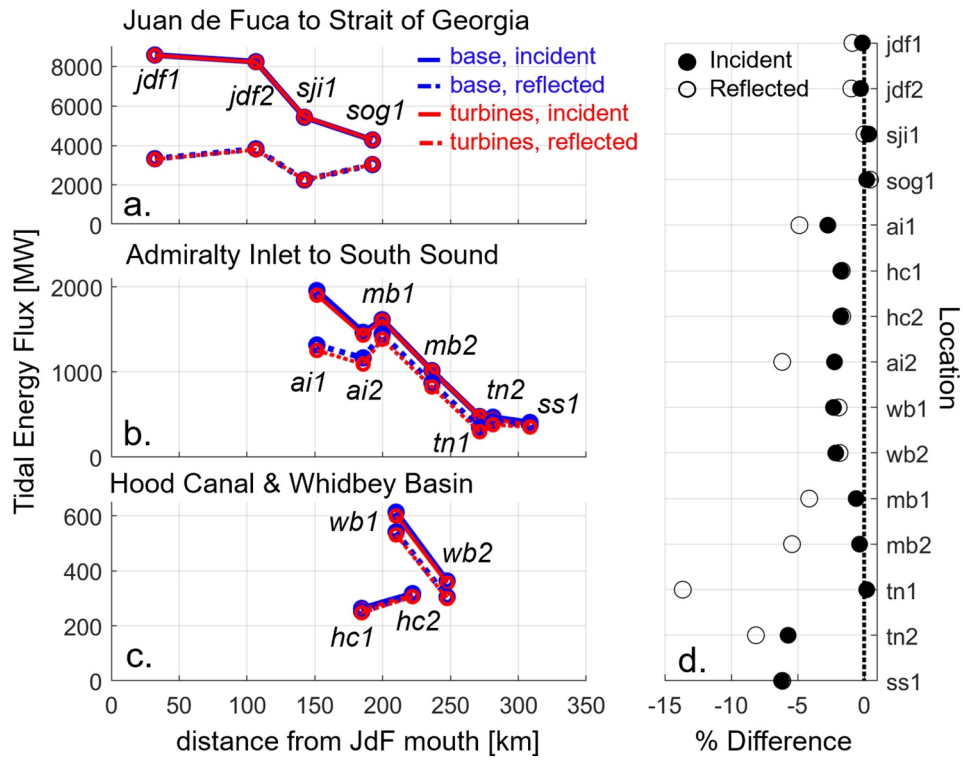

Figure 4. Same as Figure 3 but for incident (solid lines/filled circles) and reflected (dashed lines/open circles) energy fluxes. The absolute value of all reflected fluxes are shown.

of the physical mechanisms (reflection, resonance, and friction) in dictating diurnal, semidiurnal, and composite tidal modulation.

Throughout the Salish Sea, the M_2 contribution to the composite tidal energy flux dominates over K_1 for both the base and turbine cases (Figures 5a–5c, and 5e). Near the entrance to the system at *jdf1*, the base case F_{M2} is ∼3,700 MW while F_{K1} is nearly 4 times less at ∼1,000 MW (Figure 5a). Entering Puget Sound, K_1 is even less important: at *ai1* F_{M2} is 490 MW while F_{K1} is almost 9 times less at 56 MW (Figure 5c). In general, F_{M2} is 8–15 times larger than F_{K1} at all sections in Puget Sound, sub-basins included (Figures 5c and 5e). This is largely a result of M_2 tidal current amplitudes exceeding K_1 currents by upwards of 40% (Lavelle et al., 1988 and Figure 6).

The addition of turbines mainly enhances F for both frequencies within Puget Sound. F_{K1} is amplified at all locations landward of the array by up to 60% (*mb1*), while F_{M2} increases at the same locations, but to a lesser magnitude (e.g., +40% at *tn1*, Figure 5d). Both F_{M2} and F_{K1} are dampened landward of the turbine array in South Sound (−10%, *ss1*). Interestingly, in Hood Canal and Whidbey Basin, F_{K1} amplifies (e.g., +30% at *hc1*) while F_{M2} is reduced modestly (<−10% everywhere, Figure 5f). Importantly, although the K_1 tide appears slightly more sensitive than the M_2 to energy extraction, modulation to the M_2 energy flux dictates the composite tidal energy flux system wide (Figures 5b–5d, and 5f) as variation to F_{K1} is often at very minor magnitudes [$\circ(1)$ MW] relative to F_{M2} adjustments [$\circ(10)$ MW] (Figures 5a–5c and 5e). This is particularly evident in Hood Canal and Whidbey Basin, where F_{K1} increases but F_{M2} and F decrease. Incident and reflected fluxes follow suit: modulation to the composite tide F_+ and F_- is controlled primarily by the M_2 contribution (not shown).

It remains unclear how the modified tidal energy fluxes manifest in tidal characteristics. Sea surface and velocity amplitudes and phase relations control the strength of the M_2 and K_1 tidal energy fluxes (see Equations 20–22), which we present here to elucidate how the major constituents are modified by turbines thereby allowing the observed patterns in incident, reflected, and net energy fluxes. In the base case, both A_{K1} and A_{M2} are of similar magnitude system-wide and shift in dominance depending on location (Figure 6a), following expected trends outlined in Section 2. Regardless of the constituent dominating sea surface fluctuations, U_{M2} always exceeds U_{K1}, often by more than a factor of 2 (Figure 6b). When turbines are added, A_{M2} is reduced marginally from *ai2*

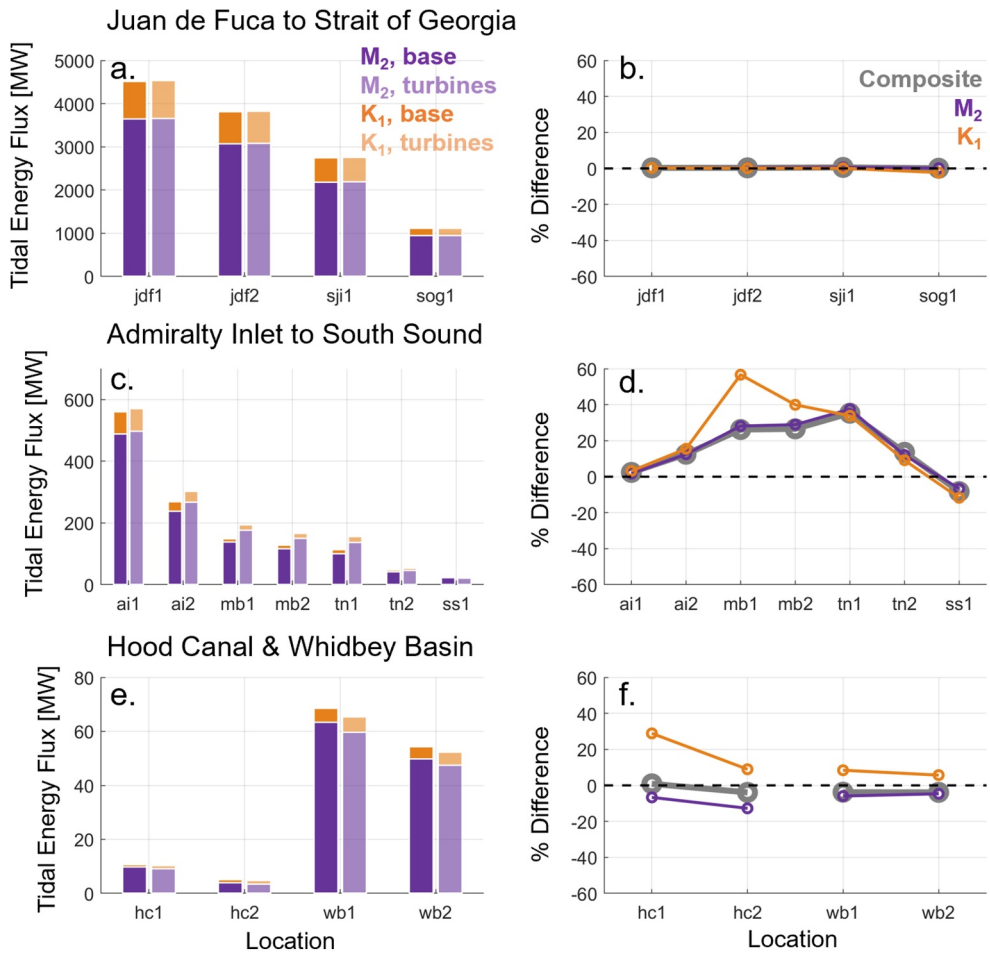

Figure 5. Contributions of M_2 (purple) and K_1 (orange) tides to composite tide energy fluxes at each section for base (dark shades) and turbine (light shades) simulations at sections in Juan de Fuca/Strait of Georgia (a), Admiralty Inlet to South Sound (c), and Hood Canal & Whidbey Basin (e). Corresponding percent differences in M_2, K_1, and composite tide energy fluxes for base case relative to turbine (b, d, f).

(~2 cm) landward to *ss1* (~5 cm) while A_{K1} is nearly unchanged except for a <1 cm reduction at *ss1* (Figure 6a). Similarly, U_{M2} is reduced slightly in the major constrictions of Admiralty Inlet (−2 cm/s at *ai1*, *ai2*) and Tacoma Narrows (−4 cm/s at *tn1*, *tn2*), while U_{K1} is unchanged (Figure 6b).

Decreases and/or no change to free surface and current amplitudes requires both the M_2 and K_1 tidal waves to transition to a more progressive-type wave to create the observed positive changes in tidal energy fluxes landward of the tidal turbines (Figure 3). Here, we compare the relative difference between incident and reflected wave amplitudes (A_-/A_+, Figure 6c) and phases ($\varphi_- - \varphi_+$, Figure 6d) to characterize the tidal wave. "Perfect" constructive interference of incident and reflected waves (i.e., a true standing wave) would occur for $A_-/A_+ = 1$ and $\varphi_- - \varphi_+ = 0$. As our simulations are realistic and include both frictional and convergent effects, this ideal condition is not met at any location (Figures 6c and 6d). Even so, in the Main Basin (*mb1*, *mb2*) and South Sound (*ss1*), the principal tides approach standing wave criteria during the base simulation, particularly the K_1 ($A_-/A_+ > 0.9$ and $\varphi_- - \varphi_+ < 45^\circ$, Figures 6c and 6d). When turbines are added, both frequencies move away from the standing wave condition between *ai1* and *tn2*, mainly via a decrease in reflected wave amplitude relative to incident: A_-/A_+ decreases by up to 5%, with the M_2 reduced more than the K_1 (Figure 6c). Interestingly, $\varphi_- - \varphi_+$ remain the same during the turbine run for both constituents (Figure 6d). Decreased F_- and increased F seaward of the array for both M_2 and K_1 is therefore attributed to attenuated reflected wave amplitudes which shift the tides further from near-standing waves toward progressive propagation. Decreased F_{M2}, F_{K1}, and F landward is a result of attenuation to *both* incident and reflected waves which dampens the free surface amplitudes. Finally,

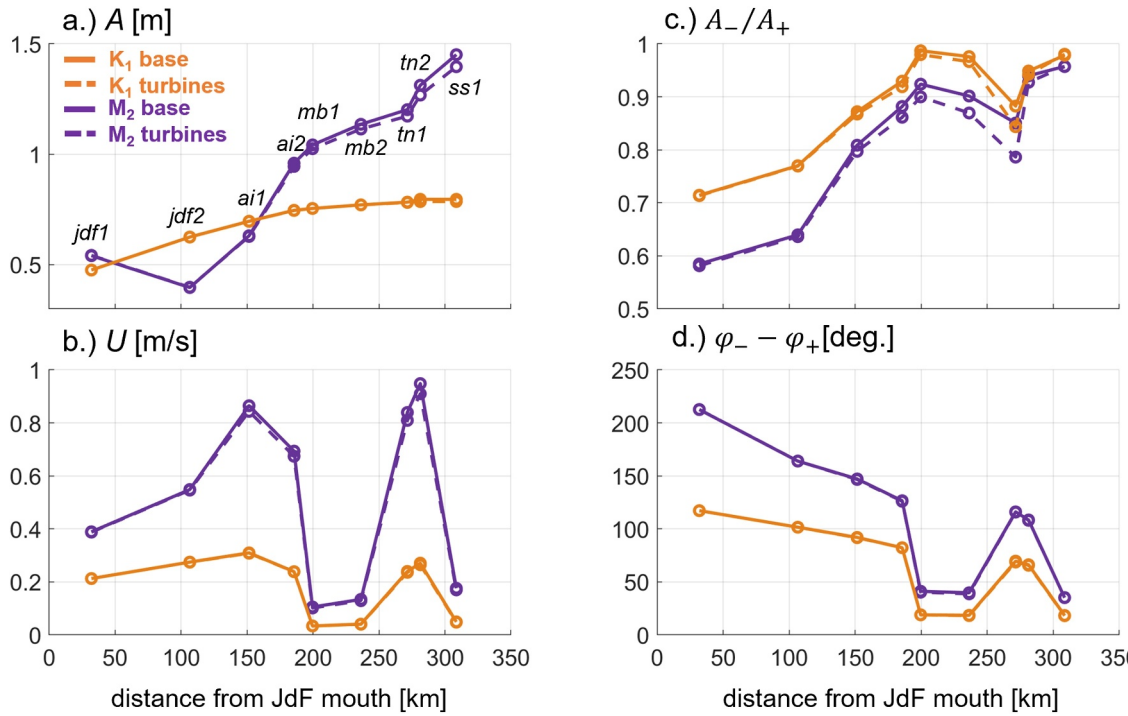

Figure 6. Section averages of M_2 (purple) and K_1 (orange) free surface amplitudes (a), section-normal current amplitudes (b), reflected/incident wave amplitude ratios (c), and reflected/incident wave phase differences (d) for base (solid lines) and turbines (dashed lines) simulations along a line from the mouth of Juan de Fuca to South Sound. Distance from the mouth of Juan de Fuca is given on the *x*-axis. Section locations are labeled in (a).

maintenance of $A_-/A_+ > 0.8$ and $\varphi_- - \varphi_+ < 90°$ over most of Puget Sound for both M_2 and K_1 suggest both frequencies are near a resonant condition.

6. Discussion

Thus far we have illustrated the addition of a large, synthetic tidal stream turbine farm in Tacoma Narrows modifies tidal energy fluxes throughout Puget Sound, predominately via modification to the M_2 amplitude and phase. The K_1 tidal energy flux, amplitude, and phase adjust similarly to the M_2, but less notably. In the following sections we aim to evaluate the relative importance of resonance and friction in dictating modulation to M_2 and K_1 tides presented here. In the absence of changes to estuary length, depth, and geometry; resonance and friction must be the main physical controls on barotropic tidal behavior (e.g., Talke & Jay, 2020). Our aim is to prove that the resonant condition is Puget Sound is modified by turbine-added frictional dissipation, and the semidiurnal and diurnal constituents respond to the added friction and resonance modifications slightly differently. We also will hypothesize as to why tidal energy fluxes are reduced in Hood Canal and Whidbey Basin and have opposing adjustments in M_2 and K_1 components, contrary to dynamics in the basins which they are connected to. Lastly, we discuss environmental implications.

6.1. Friction and Resonance in Puget Sound

Identifying the frequency response of tides in the Salish Sea, in particular the Puget Sound portion, is a useful way to understand how friction and resonance influence the dynamics of each tidal constituent. By fitting observations of tidal amplitude gain and phase differences to rectangular bay and Helmholtz resonance analytical models, Sutherland et al. (2005) identified the Juan de Fuca—Strait of Georgia system behaves closest to a Helmholtz oscillator with a resonant period near 17 hr. Helmholtz resonance differs from quarter-wavelength resonance theory for rectangular bays in that the bay is separated from open ocean forcing by a narrow channel, creating a resonant period longer than that if the connecting passage wasn't there. The Strait of Juan de Fuca and San Juan Islands are considered this narrow channel for the Strait of Georgia basin (Sutherland et al., 2005). We similarly apply both models to Puget Sound and consider Admiralty Inlet the effective tide entry point as well as the narrow

connecting strait for the Helmholtz model. Although Puget Sound in undoubtedly influenced by tidal dynamics in the much larger volume Juan de Fuca—Strait of Georgia system to which it is connected, the presence of differing tidal propagation (e.g., the M_2 amplifies more than the K_1 in Puget Sound, while the opposite holds true in the Strait of Georgia) indicates an independent frequency response is likely.

For Helmholtz resonance, the amplitude gain for a given tidal constituent can be illustrated with the analytical model:

$$\frac{A_0(L)}{A_0(0)}e^{i\varphi} = \frac{1}{1 - \frac{\omega^2}{\omega_0^2} - i\frac{\omega\lambda}{\omega_0^2}} \tag{24}$$

where $A_0(L)$ is the complex amplitude of a tide with angular frequency, ω, at the estuary head, $A_0(0)$ is the complex amplitude at the mouth, φ is the phase difference between mouth and head, ω_0 is the resonant angular frequency, and λ is a linear friction coefficient which roughly approximates quadratic friction as: $\lambda = \frac{C_D|u|}{h}$, where C_D is the quadratic bottom friction coefficient. Similarly, rectangular bay resonant amplification can be modeled with:

$$\frac{A_0(L)}{A_0(0)}e^{i\varphi} = \frac{1}{1 - \frac{\omega}{\omega_0} - \frac{1}{2}i\frac{\lambda}{\omega_0}} \tag{25}$$

Like Sutherland et al. (2005), we fit tidal elevation gains and phase differences from our numerical model output (for both the base and turbine cases) to (24) and (25) with a least squares approach as (in the case of the Helmholtz model):

$$\sum_j \sigma_j^2 = \sum_j \left| \left[\frac{A_0(L)}{A_0(0)}\right]_j e^{i\varphi_j} - \frac{1}{1 - \frac{\omega_j^2}{\omega_0^2} - i\frac{\omega_j\lambda}{\omega_0^2}} \right|^2 \tag{26}$$

with $A_0(L)$ taken from model output as a section average of A_0 at *ss1*, $A_0(0)$ taken as a section average at *ai1*, and j represents each tidal constituent. All eight constituents used to force the model were applied. ω_0 and λ were varied over a range of possible values to minimize $\sum_j \sigma_j^2$ and identify the resonant frequency.

Fitting our FVCOM output to the analytical models Equations 24 and 25 resulted in resonant periods of 10.1 and 10.2 hr, respectively, in Puget Sound for the base case which marginally increased to 10.4 and 10.3 hr for the turbine case (Figure 7). The rectangular bay model provided the best fit: $\sum_j \sigma_j^2 = 0.4$ and 0.5 for base and turbine cases, respectively, relative to $\sum_j \sigma_j^2 = 0.6$ and 0.7 for Helmholtz. The nearly identical results between both models provide some confidence in a Puget Sound resonant period of ~10 hr. The smaller resonant period than the 17-to-21-hr estimate range of Sutherland et al. (2005) for the Strait of Georgia further reinforces an independent frequency response for Puget Sound relative to the remainder of the Salish Sea, and realistic considering the smaller volume and larger M_2 amplification there.

Although resonance can be modified by several variables, the primary adjustment in this test is an increase in frictional dissipation within Tacoma Narrows. We see one result of this enhanced friction is to decrease the resonant period amplification (Figure 7). Although the theoretical resonant period is also shifted higher, it is by a nearly negligible factor (e.g., +6 min for the rectangular bay model) and hard to consider significant. Regardless, both modifications are expected: friction should slow the propagation speed of the tidal wave, thereby increasing the period, and simultaneously dissipate tidal energy, thereby reducing the maximum amplitude gain (Talke & Jay, 2020). The modified resonant condition is then expected to mainly adjust the semidiurnal frequencies, as they are much closer to resonance than the diurnal. The less-amplified resonant frequency subsequently reduces the M_2 amplification and slightly increases the phase lag (i.e., moves toward a progressive wave) (Figure 7). The K_1, being further from resonance for both scenarios, is largely unaffected by the changed resonant amplification

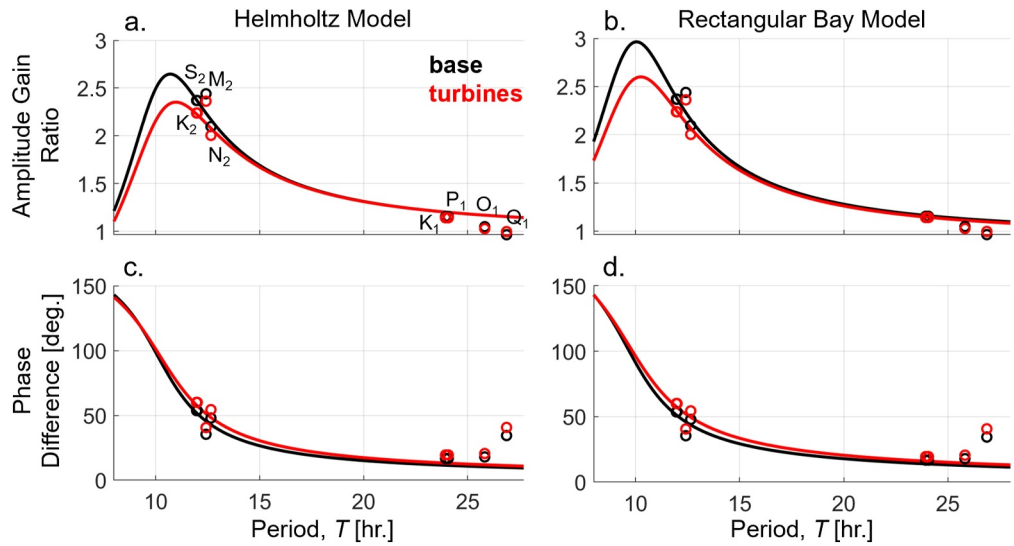

Figure 7. Frequency response of Puget Sound. Analytical model best fits (lines) were determined with numerical model output (dots). Black lines/dots denote the base simulation and red indicates the turbine simulation. The amplitude gain ratio, $\left|\frac{A_0(L)}{A_0(0)}\right|$, is given in (a, b) and the phase difference, φ, in (c, d). Helmholtz model results are in (a, c) while rectangular bay results are shown in (b, d). *X*-axis is constituent period in hours. Tidal constituents are labeled in (a).

(Figure 7). Even so, we have identified that the K_1 still experiences reduced reflection and marginally reduced amplitude in South Sound (Figure 6). The K_1 adjustments are likely more a direct result of increased frictional dissipation. Quadratic frictional damping of the tide is more effective on frequencies with weaker currents (i.e., K_1) relative to the stronger, dominant constituents (i.e., M_2) (Garrett, 1972). Thus, we assert that turbine-induced frictional dissipation is more influential on the M_2 tide (and composite tidal energy flux) because of the changed estuary resonance condition, while the K_1 is sensitive to and adjusted by friction, directly, regardless of the natural frequency.

Here we note that the analytical model results provide only an approximation of friction and resonance in the system, as shown in the non-perfect model fits, and should be interpreted as such. Puget Sound is a geographically and dynamically complex system, with topography which does not necessarily align with the simple box models applied. Even so, the decent fit of numerical output to the analytical models indicate they do describe some general features of the Puget Sound frequency response, which remains useful for this analysis, just as Sutherland et al. (2005) found utility in each model describing the complex Strait of Georgia.

Either way, the quality factor, Q, which indicates the relative importance of friction to resonance in controlling tidal dynamics supports an increase in average dissipation over the whole system due to turbines:

$$Q = \frac{\omega_0}{\lambda} \tag{27}$$

For the base simulation, $Q = 2.4$, and when turbines are added, Q decreases slightly to 2.1, indicating the average frictional dissipation (from both radiation and internal friction) over Puget Sound increases with tidal energy extraction. Indeed, λ increases from 7.3×10^{-5} to 8.1×10^{-5} s^{-1}, supporting an increase in frictional dissipation. So, although imperfect, usage of simple resonance analytical models has provided some valuable insight into how and why tidal turbines in Tacoma Narrows may modify the semidiurnal and diurnal tides over Puget Sound as a whole. A more comprehensive evaluation of segment-by-segment reflection and resonance in Puget Sound is warranted in future work.

6.2. Dynamics in Hood Canal and Whidbey Basin

Interestingly, our analysis indicates that Hood Canal and Whidbey Basin follow a different dynamical response to tidal energy extraction than the remainder of Puget Sound (Figure 5). Like other locations in Puget Sound, the K_1

tidal energy flux is enhanced in Hood Canal and Whidbey Basin (Figure 5f) due to largely similar trends in amplitude and reflection described in Figure 6 (i.e., no change to A & U, decreased reflection). Contrary to other locations, the M_2 energy flux (and therefore the composite tide F) *decreases* by 5% (Whidbey Basin) to 13% (Hood Canal, Figures 5e and 5f). Analysis of tidal amplitudes and phases in the two sub-basins suggests the M_2 tidal wave is not phase shifted at all in either sub-basin, maintains a nearly standing wave regime during both the base and turbine simulations, and sees negligible decreases in tidal current amplitudes (not shown). The turbines only act to marginally reduce the M_2 free surface amplitude by ~1 cm at *hc1*, *hc2*, *wb1*, and *wb2*, which we attribute to the modest reductions in F and F_{M2} described at those locations.

Relatively consistent modulation to the K_1 tide in all of Puget Sound's sub-basins suggests Tacoma Narrows is a dynamically consequential reflective boundary for that constituent's behavior system wide, while only regionally significant for the M_2 which is notably adjusted from Admiralty Inlet to South Sound but less so within Hood Canal and Whidbey Basin. We hypothesize that the relatively shorter (but similar) length scales of Hood Canal, Whidbey Basin (~100 km), and the main axis of Puget Sound (~160 km) favor independent (sub basin-specific) frequency responses for the shorter wavelength semidiurnal tides whereas the longer, diurnal frequencies react similarly across sub-basins. As both Hood Canal and Whidbey Basin are themselves very reflective (Mofjeld & Larsen, 1984), it is likely M_2 propagation within each is largely unconnected to dynamical adjustments at the other major reflection points in Puget Sound: Tacoma Narrows and South Sound, whereas the longer wavelength of the K_1 allows the wave to "feel" adjustments further from the turbines. More investigation on this topic is warranted in the future.

6.3. Environmental Implications and Considerations

Changing tides initiated by tidal energy extraction will modify hydrodynamics in Puget Sound and therefore has implications for the estuarine environment and ecology. The state of Washington, namely Puget Sound, is the leading producer of farmed mussels, clams, and oysters in the United States and has significant native shellfish populations which are also recreationally and commercially harvested. The economic contribution to the state from these industries was estimated to be $270 million in 2015 with employment exceeding 3,200 people (Washington Sea Grant, 2015). Intertidal mudflats and beaches are the main habitat supporting shellfish populations, with the intertidal zones of South Sound making up the majority of state shellfish production (37%) and revenue (58%). South Sound is also home to food web supporting flora and fauna such as eelgrass, often considered an indicator of estuary health (Orth et al., 2006; Waycott et al., 2009), and Chinook salmon, a major food source for many large mammals and a conduit for nutrient transfer between the Pacific Ocean and inland rivers (EPA, 2020; Washington Sea Grant, 2015). As such, the impact of tidal energy extraction on South Sound aquaculture and ecology is of particular concern.

The first order implications of our tidal energy extraction scenario on South Sound hydrodynamics are illustrated in Figure 8. In these simulations, the hypothetical turbine array in Tacoma Narrows would result in a decreased tidal range in South Sound over the full spring-neap cycle (Figure 8a). During spring tides, high (low) water elevations are nearly 10 cm less (more) when turbines are present relative to the base case, giving a tidal range reduction of nearly 20 cm (Figure 8c). Differences are less notable during neap tides, but still range from 5 to 10 cm (Figure 8c). Reductions in tidal range would create subsequent reductions in intertidal area in South Sound, habitat supportive to eelgrass and shellfish populations. Less habitat for these species could harm the shell fishing industry as well as the broader food web of the region supported by eelgrass. A recent study analyzing the effects of tidal energy extraction in a tide dominated estuary estimated a ~10% decline in intertidal area was possible with an analogous tidal range decrease of ~20 cm (Spicer et al., 2023). Similarly, we expect a reduction in the transport of water into and out of South Sound. Here, volume flux, VF, is a proxy for transport and is calculated by integrating the section normal velocity, u_*, across the channel and with depth:

$$\mathrm{VF} = \iint u_* dx\, dz \tag{28}$$

Like water levels, the magnitude of VF decreases after turbines are deployed, up to 10%, during both flood and ebb tides (Figure 8b). Maximum flood volume fluxes are ~7,000 m^3/s less than the base case during spring tides, while ebb flux magnitudes are up to 5,000 m^3/s less (Figure 8d). Dampened tidal transport into and out of South Sound could potentially have an impact on mixing and residence times within the sub-basin, important physical controls on estuarine water quality and health.

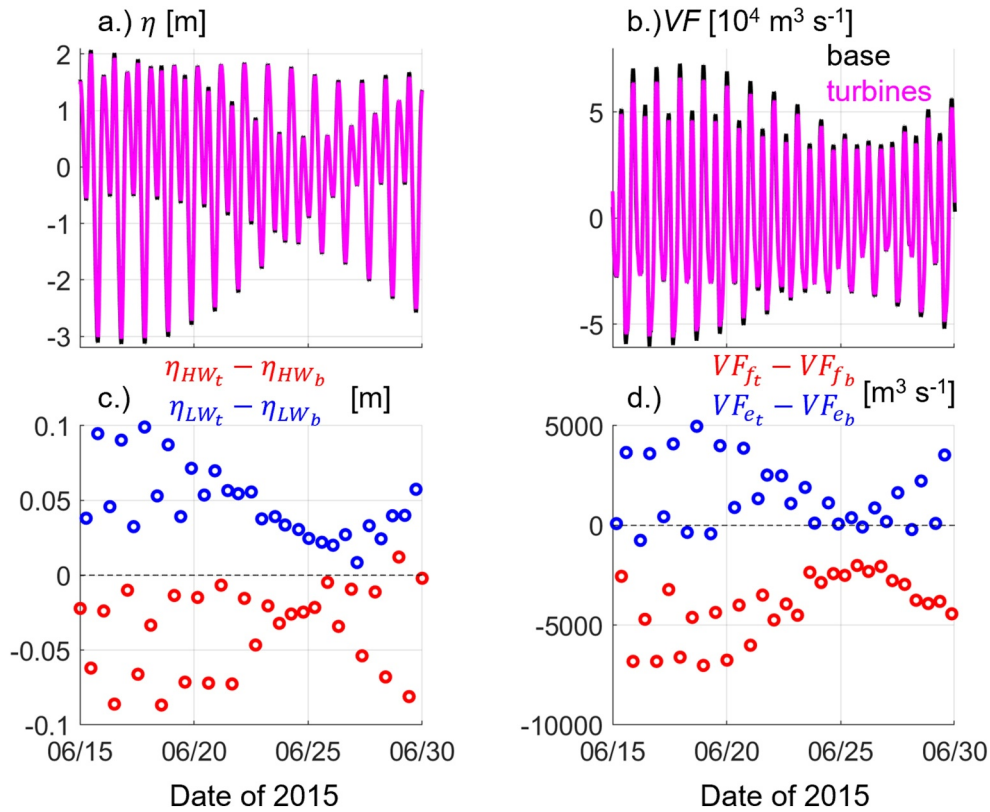

Figure 8. Time series of section averaged free surface elevation (a) and section volume flux (b) for the base (black) and turbine (magenta) simulations at *ss1* over a spring-neap cycle. Differences in high water (red) and low water (blue) elevations for each tide are given in (c), as are differences in maximum flood (red) and ebb (blue) volume fluxes in (d).

Similarly, modified tides elsewhere in Puget Sound would likely impact the spatially varying estuarine exchange flow: the major physical process connected to water quality. As dissolved oxygen levels trend downward in the Salish Sea (EPA, 2020), implications on the exchange flow are important to note. This is particularly relevant in Hood Canal, where hypoxic conditions are most prevalent and have even worsened in some locations (Newton et al., 1995), and Admiralty Inlet, which largely controls the estuarine circulation into and out of Puget Sound and its sub-basins (e.g., Geyer & Cannon, 1982; MacCready & Geyer, 2024). A comprehensive spatial analysis of exchange flows in the Salish Sea recently performed by MacCready and Geyer (2024) would suggest the reduced tidal volume transport through Admiralty Inlet would decrease internal dissipation (i.e., vertical mixing), thereby allowing stronger vertical salinity gradients, and a weaker long-term exchange flow (Figures 10 and 11 in MacCready & Geyer, 2024), both favorable conditions for worsening water quality. As these simulations omit baroclinic forcing, we cannot confirm these hypotheses, but ongoing model development will allow us to do so in the future and make more concrete conclusions. Even so, it is clear that tidal forcing is a major control on estuarine circulation and mixing nearly everywhere in the Salish Sea (MacCready & Geyer, 2024; MacCready et al., 2021), and so turbine-induced changes to tides would likely influence these processes to some degree. Elucidating the sensitivity of mixing and exchange flow to this tidal modulation is an important future topic of study.

Lastly, it is possible the presence of multiple tidal turbines in Tacoma Narrows could impact migratory fish, such as Chinook salmon, which spawn in some of the rivers and creeks discharging to South Sound. The effects of tidal turbines on migratory fish remains largely unclear, but it is known they are responsive to environmental variables such as ambient current and water quality (Polagye et al., 2011), which could be modified locally and downstream of tidal turbines. These environmental implications, amongst others, are relevant in any estuary where tidal stream turbines may be deployed and should be considered by coastal planners prior to installation.

6.4. Limitations and Open Questions

This study builds on the work of Yang et al. (2014) and Polagye et al. (2009). Yang et al. (2014) used a realistic barotropic model of the Salish Sea and found a 100-turbine array in Tacoma Narrows to modestly decrease the M_2 tidal amplitude and shift the M_2 phase within South Sound (in line with this work) but focused their analysis only on the Tacoma Narrows to South Sound region. Polagye et al. (2009) used an idealized, 1D model based broadly on the Salish Sea, and found a range of energy extraction scenarios in Tacoma Narrows could negligibly decrease the K_1 amplitude system-wide (i.e., <3%), decrease the M_2 amplitude in South Sound, and either modestly decrease or hold constant the M_2 amplitude in the Main Basin, which generally supports these results. We supplement their conclusions with a decomposition of barotropic tidal energy fluxes for both the K_1 and M_2 tides into both incident and reflected components over a full, realistic barotropic model of the Salish Sea. Further, we identified the physical mechanisms allowing modification to semidiurnal and diurnal tidal amplitude and phase: namely, changes to frictional dissipation and system resonance.

Although this work further elucidates the potential effects of localized, large scale tidal energy extraction on barotropic tides in the Salish Sea, there are limitations and further questions which should be addressed. For one, we have analyzed a single tidal stream turbine array design at one location in Puget Sound. It remains unclear how the addition of other turbine arrays, changing the dimensions of singular turbines, interactions among different turbine farms, or modifying the number of turbines in various arrays could affect tidal dynamics. More turbines in a single location always results in larger changes to hydrodynamics (e.g., Polagye et al., 2009; Yang et al., 2014), but it is not entirely clear which locations in Puget Sound are most influential to system-wide dynamics. Also, raising turbine hub heights further away from the bottom would likely place them in faster velocities and increase power extracted (by a factor of velocity magnitude, cubed) (Yang et al., 2013). This could exacerbate the hydrodynamic impact of the turbine farm. Further, energy in the M_2, K_1, and O_1 tides are not independent: they can be transferred from one constituent to the other via nonlinear advective and friction terms in the equations of motion and perhaps account for some of the varied trends in M_2 and K_1 energy fluxes described here. In this work, we assume nonlinear effects to be negligible. These limitations were considered beyond the scope of the current study but should be investigated more thoroughly in the future.

These model simulations omit the influence of baroclinic forcing on hydrodynamics. As such, the influence of internal tides and waves to energy fluxes is not included, and we are unable to analyze how tidal turbines may modify mixing and the estuarine exchange flow within the Salish Sea. These baroclinic processes are relevant and spatially variable within the Salish Sea (e.g., MacCready et al., 2021) and likely influenced to some degree by energy extraction. This remains an important open question which will allow a more comprehensive evaluation of the environmental impacts of tidal turbines on the estuarine environment. Current model development is focused on this problem.

Lastly, we note the analysis of tidal reflection and resonance in Puget Sound presented here is meant to highlight broad dynamical adjustments to M_2 and K_1 tides (and likely causation mechanisms) which could occur following a large deployment of tidal turbines in Tacoma Narrows. Due to the extreme complexity of topography and physical forcing throughout the Salish Sea, our approach carries explicit assumptions and approximations which are described in previous sections. Some of these approximations illustrate ways the reader may further develop our understanding of basic tidal propagation within the system, which we list here. (a) The Salish Sea features many regions with rapid variation in channel convergence/divergence, even though net mouth-to-head variation in convergence along a sub-basin can be quite small (see Appendix A). The role of local width variations on spatial variability in tidal propagation and resonance is unclear here but could be investigated with a comprehensive segment-by-segment evaluation of tidal wavenumber. (b) There are many sub-basins within the Salish Sea, all of which have tidal characteristics set by the sub-basin itself, as well as the larger basin it is connected to. We speculate why Hood Canal and Whidbey Basin behave differently than the Main Basin, but there is ample opportunity to apply basin-specific resonance models (e.g., Godin, 1993) which can identify the primary modulation mechanisms in each for a more holistic view of tidal interaction over the whole system. (c) A full mechanical, tidal energy budget (e.g., Giese & Jay, 1989; MacCready & Giddings, 2016) could be applied to elucidate how other tide-modulating mechanisms are adjusted following a turbine deployment and why turbines cannot account for all the change in energy dissipation within Tacoma Narrows. For example, tidal energy dissipation from *tn1* to *tn2* (the difference in F between sections, Figure 3) increases from 86 to 130 MW following turbine deployment. We calculated 70 MW of energy extraction from

the turbine array (Section 3). As the summation of 86 and 70 MW does not equal 130 MW, it can be presumed other processes are at play.

7. Conclusions

A large scale, synthetic tidal stream turbine array simulated in Tacoma Narrows has the potential to modify barotropic tidal dynamics throughout Puget Sound. Tidal energy fluxes calculated at 15 sections in the system for the base and turbine simulations indicate tidal energy extraction enhances fluxes up to 10% at the mouth of Puget Sound (Admiralty Inlet) to nearly 40% just seaward of the turbine array in Tacoma Narrows. Landward of the array in South Sound, tidal energy fluxes are decreased up to 10%, as well as in Hood Canal and Whidbey Basin. The M_2 tide is the principal constituent controlling the composite tidal energy flux due to the dominating influence of the M_2 velocity at all sections, surpassing the K_1 contribution by 1–2 orders of magnitude. Although the M_2 is shown to dictate composite tidal energy flux patterns, the K_1 tidal energy fluxes trend similarly.

We found that the tidal turbine farm increases the average frictional dissipation in Puget Sound which correspondingly adjusts the natural frequency response of the system. Changes to M_2 and K_1 tidal propagation are attributed to friction and resonance, but in differing ways. First, the enhanced dissipation of tidal energy from turbines damps the estuary resonant period (~10 hr) amplification. The M_2 tide, being relatively close to the natural period, is sensitive to this change. The reduced resonant frequency amplification increases the M_2 mouth-to-head phase lag (i.e., shifts the wave to a become more progressive) due to an attenuation of the reflected M_2 tidal wave seaward of Tacoma Narrows in Puget Sound, ultimately increasing landward energy fluxes. Further, the M_2 sea surface amplitude is dampened throughout Puget Sound but is most reduced in South Sound where both the incident and reflected waves are dampened relative to the natural condition. As such, composite tidal energy fluxes are reduced landward of the array. Although not important to composite tidal energy in Puget Sound, the K_1 is also modulated system wide. Being much further from the resonant frequency, we found the K_1 tide is largely insensitive to the adjusted resonant condition. Conversely, the K_1 *is* directly sensitive to friction as it's currents are weak relative to the M_2 and "feels" the turbine induced frictional dissipation more than the M_2. As a result, the K_1 phase lag increases seaward of Tacoma Narrows, reflected tidal energy fluxes are reduced, and the net K_1 tidal energy flux is correspondingly increased. Seaward of the turbines, the K_1 free surface amplitude and energy flux is reduced, but not as significantly as the M_2. Collectively, the modified resonant condition and subsequent adjustments to the M_2 tide initiate more significant impacts to composite tidal energy fluxes in the estuary than direct friction induced changes to K_1. We hypothesize that the reduced tidal energy fluxes in Hood Canal and Whidbey Basin, which contradict patterns in the basins they are connected to, are a result of decreased M_2 amplitudes entering each sub-basin but unchanged M_2 reflection within the basins themselves.

This work highlights the nuanced, but far-reaching effects a large-scale tidal energy extraction scenario may have on barotropic tides in large estuaries like the Salish Sea. Changing tides can result in modified intertidal zones and flood to ebb discharges, which likely effect estuarine mixing, residence times, and exchange flows. All these physical processes influence biogeochemical phenomena in estuaries which are important to water quality, aquaculture, the environment, and ecology. Careful consideration to the feedbacks between these processes is warranted prior to installing large scale tidal turbine farms in estuaries.

Appendix A: Approximating Convergence in Salish Sea Basins

For channels of exponentially converging depth and/or width, k is modified from Equation 10 following Jay (1991) to:

$$k = \frac{\omega}{\sqrt{gH}}\sqrt{(1-\Delta^2) - i\frac{\lambda}{\omega}} \tag{A1}$$

where Δ is a non-dimensional convergence parameter:

$$\Delta = \frac{\sqrt{gH}}{2L_a\omega} \tag{A2}$$

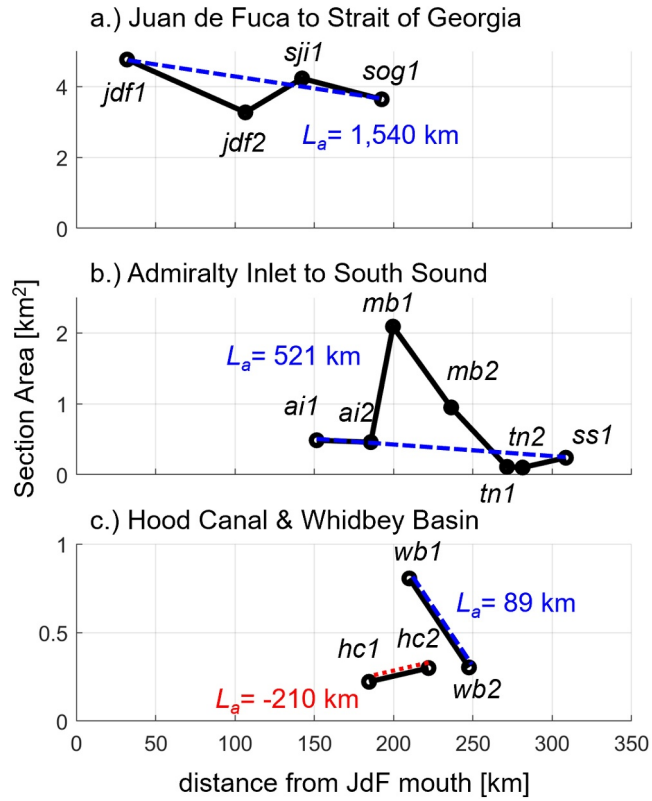

Figure A1. Cross-sectional areas of each section (y-axes) shown in Figure 1. Sections in the Straits of Juan de Fuca and Georgia are given in (a), Admiralty Inlet to South Sound in (b), and Hood Canal & Whidbey Basin in (c). Dashed blue and red lines connect the first and last section of each major basin, and the corresponding L_a estimated with those sections is shown. Red denotes diverging, blue denotes converging. Distance from the mouth of Juan de Fuca is given on the x-axis and each section is labeled.

and L_a is the e-folding length of the estuary cross-sectional area (Dykstra et al., 2023): that is, the length at which the channel cross-section has decayed to $\exp(-1) = 36.8\%$ of the area at the mouth, a_0. L_a can be estimated by fitting cross-sectional area, $a(x)$, at distance x from the mouth to: $a(x) = a_0 e^{-x/L_a}$. Equation A1 is preferrable over Equation 10 in describing tidal propagation when the added convergence term $\Delta^2 > 1$ or $L_a < \frac{\sqrt{gh}}{2\omega}$ (Jay, 1991; Talke & Jay, 2020). In that case, Equation A1 illustrates how convergence can either increase or decrease the tidal wavenumber (and therefore, speed and amplification) depending on the relative strength of friction, $i\frac{\lambda}{\omega}$. In the inviscid case, convergence always decreases k and increases the wave speed.

Here, we provide estimates of Δ^2 at each section to identify if convergence is a noteworthy mechanism modulating incident and reflected tidal waves in the Salish Sea. The Salish Sea clearly is a topographically complex estuary (Figure 1) with many sub-channels and basins of varying width and depth (Figure 1). For this reason, it is difficult to estimate L_a and Δ^2 representative of the entire system, which does not fit the idealized, exponentially converging estuary from which Equation A2 is derived. A true evaluation of convergence in the Salish Sea would likely require a segment-by-segment breakdown of many channel sections: of which defining section boundaries would be quite arbitrary. This topic is worthy of an entire study, and we believe outside the scope of this paper. Even so, estimates of convergence are possible here and warranted. To achieve this, basin specific values for L_a were estimated using the cross-sectional areas of the most landward and seaward sections in the four major basins (Figure A1). At all sections, we then calculated $\frac{\sqrt{gh}}{2\omega}$ and Δ^2 for both the M_2 and K_1 frequencies (Table A1).

Estimates indicate that Whidbey Basin is the only basin with tidal propagation modulated by convergence: $\Delta^2 > 1$ and $L_a > \frac{\sqrt{gh}}{2\omega}$ for both the M_2 and K_1 frequencies at both *wb1* and *wb2* (Table A1). The other basins: Straits of Juan de Fuca and Georgia, Puget Sound (Admiralty Inlet to South), and Hood Canal are weakly convergent, or

Table A1
Estimates for the Cross-Sectional Area e-Folding Length Scale, L_a, for Each Sub-Basin (Distinguished by Shading) With M_2 and K_1 Section-Specific Convergence Parameters: $\frac{\sqrt{gh}}{2\omega}$ and Δ

Section	L_a [km]	$\frac{\sqrt{gh}}{2\omega_{M2}}$ [km]	$\frac{\sqrt{gh}}{2\omega_{K1}}$ [km]	Δ^2_{M2}	Δ^2_{K1}
jdf1	1,540	124	240	0.08	0.16
jdf2	1,540	97	186	0.06	0.12
sji1	1,540	92	177	0.06	0.12
sog1	1,540	132	255	0.09	0.17
hc1	−210	90	175	0.43	0.83
hc2	−210	94	183	0.45	0.87
wb1	89	**140**	**269**	**1.56**	**3.01**
wb2	89	**90**	**173**	**1.01**	**1.94**
ai1	521	81	157	0.16	0.30
ai2	521	95	184	0.18	0.35
mb1	521	130	251	0.25	0.48
mb2	521	107	208	0.21	0.40
tn1	521	80	153	0.15	0.30
tn2	521	67	129	0.13	0.25
ss1	521	91	176	0.18	0.34

Note. When $L_a < \frac{\sqrt{gh}}{2\omega_{M2}}$ or $\Delta^2 > 1$, values are shown in bold.

divergent (Hood Canal) (Table A1). Even so, both converging and diverging sections occur along all basins (Figures 1 and A1) and the effect of convergence on tidal propagation throughout the system is likely highly variable in space. These estimates indicate, though, that most of the basins have mouth-to-head variability in cross-section area which is actually quite small, and justify our use of Equation 10.

Appendix B: Spatial Variability in Energy Fluxes and Comparison With Previous Work

To verify our tidal energy flux estimates are sound, we compare the composite tide net flux (F) calculated at all 15 sections to estimates from former works in the Salish Sea: namely Foreman et al. (1995) which covers Juan de Fuca and the southern Strait of Georgia, Lavelle et al. (1988) which covers Puget Sound, and the supporting information of MacCready et al. (2021) which covers the entire Salish Sea. We were also provided unpublished estimates of incident and reflected fluxes which correspond to the MacCready et al. (2021) locations to further verify our analogous results. At each location, comparisons are made between our results and those of the preceding studies. If the preceding studies did not analyze a particular location, they are omitted. The sections used in this paper were chosen as to always allow at least one of the former studies to compare with, but do not always follow the same naming convention the previous studies applied. In general, both net, incident, and reflected fluxes calculated in this work match favorably with at least one of the former studies at each section and broader trends in spatial variability (Figure B1). The largest differences occur in the Main Basin between the MacCready et al. (2021) estimates relative to ours and those of Lavelle et al. (1988), which are 20%–30% smaller. It is possible the MacCready et al. (2021) overestimations result from baroclinicity in their model, which differs from the barotropic approach of this work and Lavelle et al. (1988).

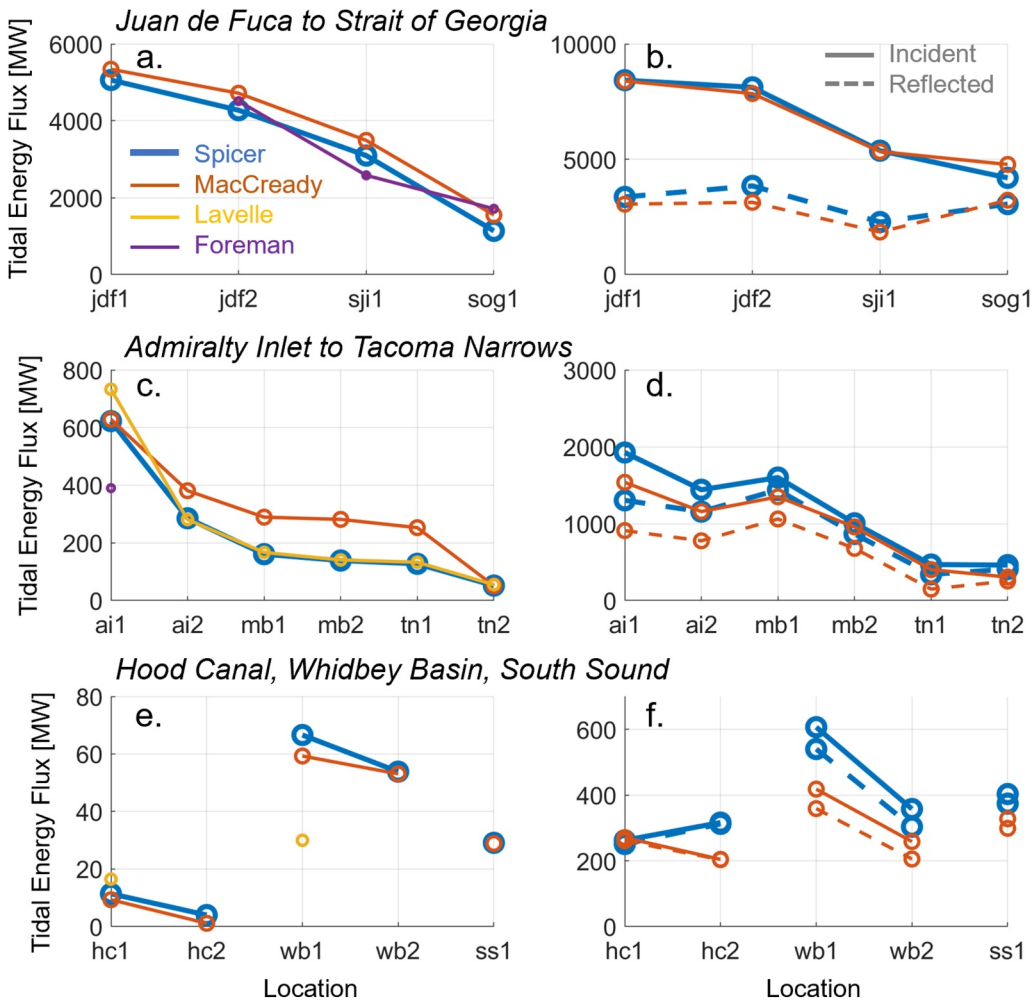

Figure B1. Comparison of net (left panels) and incident/reflected (right panels) tidal energy flux estimates from this paper (blue) compared to MacCready et al. (2021) (orange), Lavelle et al. (1988) (yellow), and Foreman et al. (1995) (purple) at sections in Juan de Fuca/Strait of Georgia (a, b), Admiralty Inlet to Tacoma Narrows (c, d), and Hood Canal, Whidbey Basin, and South Sound (e, f). Section names are given on the *x*-axis and energy flux, in megawatts, on the *y*-axis. The absolute value of reflected energy fluxes are shown as dashed lines in the right panels while incident energy fluxes are solid lines.

Acknowledgments
This study was funded by the U.S. Department of Energy, Office of Energy Efficiency and Renewable Energy, Water Power Technologies Office on tidal energy resource characterization under contract DE-AC05-76RL01830 to Pacific Northwest National Laboratory. All colormaps were created with the cmocean MATLAB toolbox (Thyng et al., 2016). Model simulations were performed using the Constance Computing System at Pacific Northwest National Laboratory and the Eagle Computing System at the National Renewable Energy Laboratory. The authors would like to thank Hal Mofjeld for the formulation used in decomposing a tidal wave into incident and reflected components, and for providing comments on an earlier version of this manuscript. The authors also thank Chris Garrett, Mike Foreman, and David Jay for thorough, constructive reviews which greatly improved the original manuscript.

Data Availability Statement

The hydrodynamic model used in this study is the publicly available Finite Volume Community Ocean Model (FVCOM, Chen et al., 2003). All data used in the paper are available from https://doi.org/10.5281/zenodo.10783531 (Spicer, 2024).

References

Allen, G. P., Salomon, J. C., Bassoullet, P., Du Penhoat, Y., & de Grandpré, C. (1980). Effects of tides on mixing and suspended sediment transport in macrotidal estuaries. *Sedimentary Geology*, *26*(1), 69–90. https://doi.org/10.1016/0037-0738(80)90006-8

Bretschneider, D. E., Cannon, G. A., Holbrook, J. R., & Pashinski, D. J. (1985). Variability of subtidal current structure in a fjord estuary: Puget Sound, Washington. *Journal of Geophysical Research*, *90*(C6), 11949–11958. https://doi.org/10.1029/JC090iC06p11949

Burchard, H., Schuttelaars, H. M., & Ralston, D. K. (2018). Sediment trapping in estuaries. *Annual Review of Marine Science*, *10*(1), 371–395. https://doi.org/10.1146/annurev-marine-010816-060535

Chen, C., Liu, H., & Beardsley, R. C. (2003). An unstructured grid, finite-volume, three-dimensional, primitive equations ocean model: Application to coastal ocean and estuaries. *Journal of Atmospheric and Oceanic Technology*, *20*(1), 159–186. https://doi.org/10.1175/1520-0426(2003)020<0159:AUGFVT>2.0.CO;2

Codiga, D. L. (2011). Unified tidal analysis and prediction using the UTide Matlab Functions. Retrieved from ftp://www.po.gso.uri.edu/pub/downloads/codiga/pubs/2011Codiga-UTide-Report.pdf

Cowles, G. W., Hakim, A. R., & Churchill, J. H. (2017). A comparison of numerical and analytical predictions of the tidal stream power resource of Massachusetts, USA. *Renewable Energy*, *114*, 215–228. https://doi.org/10.1016/j.renene.2017.05.003

Curl, H., & Paulson, A. (1991). The biochemistry of oxygen and nutrients in Hood Canal. In *Puget sound Research'91 proceedings*.
De Dominicis, M., O'Hara Murray, R., & Wolf, J. (2017). Multi-scale ocean response to a large tidal stream turbine array. *Renewable Energy*, *114*, 1160–1179. https://doi.org/10.1016/j.renene.2017.07.058
Defne, Z., Haas, K. A., Fritz, H. M., Jiang, L., French, S. P., Shi, X., et al. (2012). National geodatabase of tidal stream power resource in USA. *Renewable and Sustainable Energy Reviews*, *16*(5), 3326–3338. https://doi.org/10.1016/j.rser.2012.02.061
Doodson, A. T. (1921). The harmonic development of the tide-generating potential. *Proceedings of the Royal Society of London - Series A: Containing Papers of a Mathematical and Physical Character*, *100*(704), 305–329.
Dyer, K. R. (1995). Chapter 14 sediment transport processes in estuaries. In G. M. E. Perillo (Ed.), *Developments in sedimentology* (Vol. 53, pp. 423–449). Elsevier. https://doi.org/10.1016/S0070-4571(05)80034-2
Dykstra, S. L., Viparelli, E., Talke, S. A., Yankovsky, A. E., & Torres, R. (2023). Reflection of storm surge and tides in convergent estuaries with dams, the case of Charleston, USA. *ESS Open Archive*. https://doi.org/10.22541/essoar.169566471.14600829/v1
Ebbesmeyer, C. C., & Barnes, C. A. (1980). Control of a fjord basin's dynamics by tidal mixing in embracing sill zones. *Estuarine and Coastal Marine Science*, *11*(3), 311–330. https://doi.org/10.1016/S0302-3524(80)80086-7
Edwards, K. A., MacCready, P., Moum, J. N., Pawlak, G., Klymak, J. M., & Perlin, A. (2004). Form drag and mixing due to tidal flow past a sharp point. *Journal of Physical Oceanography*, *34*(6), 1297–1312. https://doi.org/10.1175/1520-0485(2004)034<1297:fdamdt>2.0.co;2
EPA. (2020). Health of the Salish Sea ecosystem report. Retrieved from https://www.epa.gov/salish-sea
Foreman, M. G. G., & Henry, R. F. (1989). The harmonic analysis of tidal model time series. *Advances in Water Resources*, *12*(3), 109–120. https://doi.org/10.1016/0309-1708(89)90017-1
Foreman, M. G. G., Walters, R. A., Henry, R. F., Keller, C. P., & Dolling, A. G. (1995). A tidal model for eastern Juan de Fuca Strait and the southern Strait of Georgia. *Journal of Geophysical Research*, *100*(C1), 721–740. https://doi.org/10.1029/94jc02721
Garrett, C. (1972). Tidal resonance in the bay of fundy and Gulf of Maine. *Nature*, *238*(5365), 441–443. https://doi.org/10.1038/238441a0
Garrett, C., & Cummins, P. (2005). The power potential of tidal currents in channels. *Proceedings of the Royal Society A: Mathematical, Physical and Engineering Sciences*, *461*(2060), 2563–2572. https://doi.org/10.1098/rspa.2005.1494
Geyer, W. R., & Cannon, G. A. (1982). Sill processes related to deep water renewal in a fjord. *Journal of Geophysical Research*, *87*(C10), 7985–7996. https://doi.org/10.1029/JC087iC10p07985
Geyer, W. R., & MacCready, P. (2014). The estuarine circulation. *Annual Review of Fluid Mechanics*, *46*(1), 175–197. https://doi.org/10.1146/annurev-fluid-010313-141302
Geyer, W. R., & Smith, J. D. (1987). Shear instability in a highly stratified estuary. *Journal of Physical Oceanography*, *17*(10), 1668–1679. https://doi.org/10.1175/1520-0485(1987)017<1668:siiahs>2.0.co;2
Giese, B. S., & Jay, D. A. (1989). Modelling tidal energetics of the Columbia river estuary. *Estuarine, Coastal and Shelf Science*, *29*(6), 549–571. https://doi.org/10.1016/0272-7714(89)90010-3
Godin, G. (1986). The use of nodal corrections in the calculation of harmonic constants. *International Hydrographic Review*.
Godin, G. (1993). On tidal resonance. *Continental Shelf Research*, *13*(1), 89–107. https://doi.org/10.1016/0278-4343(93)90037-X
Haas, K. A., Fritz, H. M., French, S. P., Smith, B. T., & Neary, V. S. (2011). Assessment of energy production potential from tidal streams in the United States. https://doi.org/10.2172/1219367
Hasegawa, D., Sheng, J., Greenberg, D. A., & Thompson, K. R. (2011). Far-field effects of tidal energy extraction in the Minas Passage on tidal circulation in the Bay of Fundy and Gulf of Maine using a nested-grid coastal circulation model. *Ocean Dynamics*, *61*(11), 1845–1868. https://doi.org/10.1007/s10236-011-0481-9
Haverson, D., Bacon, J., Smith, H. C. M., Venugopal, V., & Xiao, Q. (2018). Modelling the hydrodynamic and morphological impacts of a tidal stream development in Ramsey Sound. *Renewable Energy*, *126*, 876–887. https://doi.org/10.1016/j.renene.2018.03.084
IEC. (2015). *Technical specification: Marine energy—wave, tidal and other water current converters - Part 201: Tidal energy resource assessment and characterization*. In (Vol. IEC TS 62600–201, pp. 44).
Jay, D. A. (1991). Green's law revisited: Tidal long-wave propagation in channels with strong topography. *Journal of Geophysical Research*, *96*(C11), 20585–20598. https://doi.org/10.1029/91JC01633
Kilcher, L., Thresher, R., & Tinnesand, H. (2016). Marine hydrokinetic energy site identification and ranking methodology part II: Tidal energy.
Lavelle, J. W., Mofjeld, H. O., Lempriere-Doggett, E., Cannon, G. A., Pashinski, D. J., Cokelet, E. D., et al. (1988). *A multiply-connected channel model of tides and tidal currents in Puget Sound, Washington and a comparison with updated observations*. NOAA Technical Memorandum, Issue. N. T. I. Service.
LeBlond, P. H. (1983). The Strait of Georgia: Functional anatomy of a coastal sea. *Canadian Journal of Fisheries and Aquatic Sciences*, *40*(7), 1033–1063. https://doi.org/10.1139/f83-128
Li, X., Li, M., McLelland, S. J., Jordan, L.-B., Simmons, S. M., Amoudry, L. O., et al. (2017). Modelling tidal stream turbines in a three-dimensional wave-current fully coupled oceanographic model. *Renewable Energy*, *114*, 297–307. https://doi.org/10.1016/j.renene.2017.02.033
MacCready, P., & Geyer, W. R. (2024). Estuarine exchange flow in the Salish Sea. *Journal of Geophysical Research: Oceans*, *129*(1), e2023JC020369. https://doi.org/10.1029/2023JC020369
MacCready, P., & Giddings, S. N. (2016). The mechanical energy budget of a regional ocean model. *Journal of Physical Oceanography*, *49*(9), 2719–2733. https://doi.org/10.1175/JPO-D-16-0086.1
MacCready, P., McCabe, R. M., Siedlecki, S. A., Lorenz, M., Giddings, S. N., Bos, J., et al. (2021). Estuarine circulation, mixing, and residence times in the Salish Sea. *Journal of Geophysical Research: Oceans*, *126*(2), e2020JC016738. https://doi.org/10.1029/2020JC016738
MacCready, P., Pawlak, G., Edwards, K., & McCabe, R. (2003). Form drag on ocean flows. Near boundary processes and their parameterization. In *Proceedings of 13th'Aha Huliko'a Hawaiian winter workshop*.
McCabe, R. M., MacCready, P., & Pawlak, G. (2006). Form drag due to flow separation at a headland. *Journal of Physical Oceanography*, *36*(11), 2136–2152. https://doi.org/10.1175/jpo2966.1
Mellor, G. L., & Yamada, T. (1982). Development of a turbulence closure model for geophysical fluid problems [Review]. *Reviews of Geophysics*, *20*(4), 851–875. https://doi.org/10.1029/RG020i004p00851
Mofjeld, H. O., & Larsen, L. H. (1984). Tides and tidal currents of the inland waters of western Washington.
Newton, J., Thomson, A., Eisner, L., Hannach, G., & Albertson, S. (1995). Dissolved oxygen concentrations in Hood canal: Are conditions different than forty years ago. In *Puget sound research '95 proceedings, Puget sound water quality authority, Olympia, Washington* (pp. 1002–1008).
O'Hara Murray, R., & Gallego, A. (2017). A modelling study of the tidal stream resource of the Pentland Firth, Scotland. *Renewable Energy*, *102*, 326–340. https://doi.org/10.1016/j.renene.2016.10.053

Orth, R. J., Carruthers, T. J. B., Dennison, W. C., Duarte, C. M., Fourqurean, J. W., Heck, K. L., et al. (2006). A global crisis for seagrass ecosystems. *BioScience*, *56*(12), 987–996. https://doi.org/10.1641/0006-3568(2006)56[987:Agcfse]2.0.Co;2

Paulson, A. J., Konrad, C. P., Frans, L. M., Noble, M., Kendall, C., Josberger, E. G., et al. (2006). *Freshwater and saline loads of dissolved inorganic nitrogen to Hood Canal and Lynch Cove*. Scientific Investigations Report. U. S. Geological Survey.

Polagye, B., Kawase, M., & Malte, P. (2009). In-stream tidal energy potential of Puget Sound, Washington. *Proceedings of the Institution of Mechanical Engineers, Part A: Journal of Power and Energy*, *223*(5), 571–587. https://doi.org/10.1243/09576509JPE748

Polagye, B., Van Cleve, B., Copping, A., & Kirkendall, K. (Eds.) (2011)., *Environmental effects of tidal energy development* (p. 186). U.S. Department Commerce, NOAA Tech. Memorandum NMFS F/SPO-116.

Rao, S., Xue, H., Bao, M., & Funke, S. (2016). Determining tidal turbine farm efficiency in the Western Passage using the disc actuator theory. *Ocean Dynamics*, *66*(1), 41–57. https://doi.org/10.1007/s10236-015-0906-y

Sánchez, M., Carballo, R., Ramos, V., & Iglesias, G. (2014). Tidal stream energy impact on the transient and residual flow in an estuary: A 3D analysis. *Applied Energy*, *116*, 167–177. https://doi.org/10.1016/j.apenergy.2013.11.052

Sleath, J. (1987). Turbulent oscillatory flow over rough beds. *Journal of Fluid Mechanics*, *182*(-1), 369–409. https://doi.org/10.1017/s0022112087002374

Smagorinsky, J. (1963). General circulation experiments with the primitive equations: I. The basic experiment. *Monthly Weather Review*, *91*(3), 99–164. https://doi.org/10.1175/1520-0493(1963)091<0099:GCEWTP>2.3.CO;2

Spicer, P. (2024). Supporting data for figures in "localized, tidal energy extraction in Puget Sound can adjust estuary resonance and friction, modifying barotropic tides system-wide" (version 4) [Dataset]. *Zenodo*. https://doi.org/10.5281/zenodo.10783531

Spicer, P., Yang, Z., Wang, T., & Deb, M. (2023). Tidal energy extraction modifies tidal asymmetry and transport in a shallow, well-mixed estuary. *Frontiers in Marine Science*, *10*(10). https://doi.org/10.3389/fmars.2023.1268348

Sutherland, D. A., MacCready, P., Banas, N. S., & Smedstad, L. F. (2011). A model study of the Salish Sea estuarine circulation. *Journal of Physical Oceanography*, *41*(6), 1125–1143. https://doi.org/10.1175/2011JPO4540.1

Sutherland, G., Foreman, M., & Garrett, C. (2007). Tidal current energy assessment for Johnstone Strait, Vancouver Island. *Proceedings of the Institution of Mechanical Engineers, Part A: Journal of Power and Energy*, *221*(2), 147–157. https://doi.org/10.1243/09576509JPE338

Sutherland, G., Garrett, C., & Foreman, M. (2005). Tidal Resonance in Juan de Fuca Strait and the Strait of Georgia. *Journal of Physical Oceanography*, *35*(7), 1279–1286. https://doi.org/10.1175/JPO2738.1

Talke, S. A., & Jay, D. A. (2020). Changing tides: The role of natural and anthropogenic factors. *Annual Review of Marine Science*, *12*(1), 121–151. https://doi.org/10.1146/annurev-marine-010419-010727

Thomson, R. E. (1981). Oceanography of the British Columbia coast. *Canadian Special Publication of Fisheries and Aquatic Sciences*, *50*, 1–291.

Thomson, R. E., Mihály, S. F., & Kulikov, E. A. (2007). Estuarine versus transient flow regimes in Juan de Fuca Strait. *Journal of Geophysical Research*, *112*(C9). https://doi.org/10.1029/2006JC003925

Thyng, K. M., Greene, C. A., Hetland, R. D., Zimmerle, H. M., & DiMarco, S. F. (2016). True colors of oceanography: Guidelines for effective and accurate colormap selection. *Oceanography*, *29*(3), 9–13. https://doi.org/10.5670/oceanog.2016.66

Wang, T., & Yang, Z. (2017). A modeling study of tidal energy extraction and the associated impact on tidal circulation in a multi-inlet bay system of Puget Sound. *Renewable Energy*, *114*, 204–214. https://doi.org/10.1016/j.renene.2017.03.049

Ward, S. L., Green, J. A. M., & Pelling, H. E. (2012). Tides, sea-level rise and tidal power extraction on the European shelf. *Ocean Dynamics*, *62*(8), 1153–1167. https://doi.org/10.1007/s10236-012-0552-6

Washington Sea Grant. (2015). Shellfish aquaculture in Washington state (final report to the Washington state Legislature, issue.

Waycott, M., Duarte, C. M., Carruthers, T. J. B., Orth, R. J., Dennison, W. C., Olyarnik, S., et al. (2009). Accelerating loss of seagrasses across the globe threatens coastal ecosystems. *Proceedings of the National Academy of Sciences of the United States of America*, *106*(30), 12377–12381. https://doi.org/10.1073/pnas.0905620106

Woodson, C. B. (2018). The fate and impact of internal waves in nearshore ecosystems. *Annual Review of Marine Science*, *10*(1), 421–444. https://doi.org/10.1146/annurev-marine-121916-063619

Yang, Z., Wang, T., Branch, R., Xiao, Z., & Deb, M. (2021). Tidal stream energy resource characterization in the Salish Sea. *Renewable Energy*, *172*, 188–208. https://doi.org/10.1016/j.renene.2021.03.028

Yang, Z., Wang, T., Copping, A., & Geerlofs, S. (2014). Modeling of in-stream tidal energy development and its potential effects in Tacoma Narrows, Washington, USA. *Ocean & Coastal Management*, *99*, 52–62. https://doi.org/10.1016/j.ocecoaman.2014.02.010

Yang, Z., Wang, T., & Copping, A. E. (2013). Modeling tidal stream energy extraction and its effects on transport processes in a tidal channel and bay system using a three-dimensional coastal ocean model. *Renewable Energy*, *50*, 605–613. https://doi.org/10.1016/j.renene.2012.07.024